

HIGH-PERFORMANCE ANTENNA DESIGN FOR IOT, WEARABLE, AND 5G  
COMMUNICATIONS

By

TONMOY KUMAR SAHA

A thesis submitted in partial fulfillment of  
the requirements for the degree of

MASTER OF SCIENCE IN ELECTRICAL ENGINEERING

WASHINGTON STATE UNIVERSITY  
School of Engineering and Computer Science, Vancouver

MAY 2019

© Copyright by TONMOY KUMAR SAHA, 2019  
All Rights Reserved



To the Faculty of Washington State University:

The members of the Committee appointed to examine the thesis of TONMOY KUMAR SAHA find it satisfactory and recommend that it be accepted.

---

Praveen Sekhar, Ph.D., Chair

---

Tutku Karacolak, Ph.D.

---

Jong-Hoon Kim, Ph.D.

## **ACKNOWLEDGMENT**

First and foremost, I want to express my deep and sincere gratitude to my advisor, Dr. Praveen Sekhar, for his continuous support, and encouragement throughout my graduate-level study and research. I appreciate, he continually and convincingly conveyed a spirit of adventure to explore new ideas without being afraid of failure. Without his guidance and persistent help as a great mentor, this dissertation would not have been possible.

My earnest thanks to Dr. Tutku Karacolak, who provided me lots of good advice and supported in antenna design and analysis throughout my masters' program. I would like to thank Dr. Jong-Hoon Kim for being my committee members and giving suggestions on my thesis. Additionally, I would like to thank my course instructors, and academic staffs for their valuable materials, time, and consideration.

Special thanks to Hashem and Sayem, who went through hard times together with me, cheered me on, celebrated each accomplishment, and managed to make me feel special. I am also very grateful to all WSU Vancouver and local friends who have given me a wonderful time, support, and suggestions without you, life would have been boring.

Finally, I have to thank my loving parents and each member of my family for their continuous support, and encouragement throughout for my life. I owe thanks to a special person, my wife for her love, emotional support, and understanding. I greatly value her contribution and sincerely appreciate her belief in me.

HIGH-PERFORMANCE ANTENNA DESIGN FOR IOT, WEARABLE, AND 5G  
COMMUNICATIONS

**Abstract**

by Tonmoy Kumar Saha, M.S.  
Washington State University  
May 2019

Chair: Praveen Sekhar

Advances in ubiquitous antenna technology is driven by the continuous demand for Internet of Things (IoT) products. To date, the industry has been addressing these demands by enhancing the signaling strength, speed, operating bandwidth, etc which facilitated different generations of wireless technology (1G, 2G, 3G, 4G, and 5G). Several unintended factors have undermined the benefit from the advances in flexible inkjet printed Antenna of Things (AoT) products. Notably, the challenges associated with these are to maintain constant conductive performance at flexible or reconfigurable conditions. Previous studies emphasized more on the design improvements instead of establishing an ideal printing condition for antenna implementation. This research aims to establish a unique, and cost-effective inkjet printing properties on the photo paper using silver nano ink. This step is followed by the fabrication of an antenna and comparing the response with relatively similar antenna architecture with the rigid FR4 substrate. After printing optimization, and fabrication, the flexible printed pattern was subjected to several repetitive rolling and bending test. The results confirm the robustness of the specimen. Since a single ultra-wideband (UWB) antenna can replace many single narrow-banded antennas, a UWB antenna was implemented on photo paper with the optimized printing methods. The

antenna operates over 3.2–30 GHz frequency range and compliant with UWB standards. Finally, a new 5G phased array antenna design is proposed in order to keep pace with the future IoT and high-speed 5G communication.

## TABLE OF CONTENTS

	Page
ACKNOWLEDGMENT.....	iii
ABSTRACT.....	iv
LIST OF TABLES.....	ix
LIST OF FIGURES.....	x
CHAPTER 1: INTRODUCTION.....	1
1.1 Background.....	1
1.2 Inkjet printing.....	2
1.3 Ultra wideband (UWB) antennas.....	3
1.4 5G Antenna.....	4
1.5 Motivation and Research Goals.....	5
1.6 Thesis Organization.....	6
CHAPTER 2: INVESTIGATION OF PRINTING PROPERTIES ON PAPER SUBSTRATE....	9
2.1 Background.....	9
2.2 Experimental.....	10
2.2.1 Printing.....	10
2.2.2 Sintering (Heat Treatment).....	14
2.2.3 Resistivity Measurements.....	14

2.2.4	Flexibility Test .....	15
2.2.5	Surface Roughness Measurement and Surface Characterization.....	15
2.3	Results and Discussion.....	15
2.3.1	Sintering and Resistivity Results .....	15
2.3.2	Surface Characterization.....	18
2.4	Summary .....	23
CHAPTER 3 : A CPW-Fed Flexible UWB Antenna for IoT Applications .....		24
3.1	Background .....	24
3.2	Structure of the Antenna Design .....	25
3.3	Antenna Fabrication .....	27
3.4	Results and Discussion.....	30
3.5	Summary .....	37
CHAPTER 4: A COMPACT MONOPOLE ANTENNA FOR ULTRA-WIDEBAND (UWB) APPLICATIONS .....		38
4.1	Background .....	38
4.2	Structure of the antenna design .....	39
4.3	Results and discussion.....	42
4.4	Summary .....	48

CHAPTER 5: BEAM-STEERABLE MODIFIED BOW-TIE ANTENNA ARRAY FOR 5G COMMUNICATIONS .....	49
5.1 Background .....	49
5.2 Single element modified bow-tie antenna.....	50
5.3 The proposed beam-steerable antenna array design:.....	56
5.4 Summary .....	62
CHAPTER 6: CONCLUSIONS AND FUTURE WORK.....	63
REFERENCES .....	65

## LIST OF TABLES

	Page
<b>Table 2.1</b> Optimal printing parameters .....	11
<b>Table 2.2</b> Resistivity results at different curing conditions and drop spacing .....	16
<b>Table 2.3</b> ANOVA Analysis .....	17
<b>Table 2.4</b> Layer thickness of the printed patterns .....	20
<b>Table 2.5</b> Average roughness of 3 different printed layer samples .....	21
<b>Table 3.1</b> Optimized dimensions of the proposed paper antenna. ....	26
<b>Table 4.1.</b> Optimized dimensions of the designed UWB antenna .....	41
<b>Table 5.1.</b> Optimized dimensions of proposed 5G antenna .....	52

## LIST OF FIGURES

	Page
<b>Figure 1.1.</b> Details of the Fujifilm's Dimatix Inkjet Printer, DMP 2831 .....	3
<b>Figure 1.2.</b> Spectrum of UWB signal compared with narrowband Signal [15].....	4
<b>Figure 2.1.</b> Inkjet printing process .....	12
<b>Figure 2.2.</b> Image of the sample printed pattern acquired with a) digital camera, b) Fiducial Camera of DMP. ....	13
<b>Figure 2.3.</b> Resistivity result of samples with different curing temperatures. The error bar represents standard deviation. (Number of printed layers, 1L: One layer, 2L: Two Layer, and 3L: Three Layer).....	17
<b>Figure 2.4.</b> CD microscopy images to observe ink deposition, holes, crack, and coffee ring effect at 10X magnification level. The printed samples are: (a) single layer, air cure, (b) single layer, cured at 90 °C, (c) double layer, air cure, (d) double layer, cured at 90 °C, (e) triple layer, air cure, and (f) triple layer, cured at 120 °C.....	18
<b>Figure 2.5.</b> Thickness of double-layer printed samples using SEM. ....	19
<b>Figure 2.6.</b> Surface roughness analysis using the Optical Profiler of (a) Single layer, (b) Double layer, and (c) Triple layer printed samples. ....	20
<b>Figure 2.7.</b> SEM pictures for microstructural variations on the pattern surface as a function of number of printed layers and sintering temperature. The effect of amount of layer printed and cured	

at 90 °C for a (a) single layer, (b) double layer, and (c) triple layer sample. Surface morphology of double layer printed pattern sintered at (d) 60 °C, (e) 90 °C, and (f) 120 °C..... 22

**Figure 2.8.** Bending test using (a) cylindrical shape structure and (b) hand..... 23

**Figure 3.1.** The geometry of the proposed UWB paper antenna. (a) Top view of the designed antenna, (b) Side view of the antenna looking from the feeding end, and (c) Portions of the down stepped ground plane. .... 25

**Figure 3.2.** Inkjet printed antenna on the paper substrate with silver nanoparticles ink. (a) During printing utilizing Fujifilm’s Dimatix 2831 inkjet printer, (b) The prototype of the printed antenna (darkish brown color, before curing), and (c) Fabricated tan colored of the same antenna after curing. .... 28

**Figure 3.3.** Surface morphology of the printed pattern after sintering. (a) Compound microscopy (CD) image of the printed pattern and the surface to observe any ink deposition, holes, crack, and coffee ring effect at 10X magnification level, and (b) SEM image of the microstructural variations of the printed silver nanoparticles ink on the paper substrate at 20000X magnification level. .... 29

**Figure 3.4.** The CPW-fed fabricated UWB paper antenna. .... 30

**Figure 3.5.** Simulated reflection coefficient in dB of the proposed antenna as a function of frequency..... 30

**Figure 3.6.** Simulated and measured reflection coefficients in dB of the proposed antenna as a function of frequency..... 31

**Figure 3.7.** Simulated peak gain plot as a function of frequency..... 32

<b>Figure 3.8.</b> Simulated radiation efficiency plot as a function of frequency.....	33
<b>Figure 3.9.</b> Simulated radiation pattern of the antenna at 4.0 GHz for a) $\varphi = 0^\circ$ and b) $\varphi = 90^\circ$ planes. ....	34
<b>Figure 3.10.</b> Simulated radiation pattern of the antenna at 6.2 GHz for a) $\varphi = 0^\circ$ and b) $\varphi = 90^\circ$ planes. ....	34
<b>Figure 3.11.</b> Simulated radiation pattern of the antenna at 9.2 GHz for a) $\varphi = 0^\circ$ and b) $\varphi = 90^\circ$ planes. ....	35
<b>Figure 3.12.</b> Simulated radiation pattern of the antenna at 26.0 GHz for a) $\varphi = 0^\circ$ and b) $\varphi = 90^\circ$ planes. ....	35
<b>Figure 3.13.</b> Bending test (a) deformed using human hand and (b) roll bending .....	36
<b>Figure 4.1.</b> Geometry of the designed antenna .....	40
<b>Figure 4.2.</b> The fabricated UWB antenna .....	42
<b>Figure 4.3.</b> Simulated return loss of the designed antenna .....	43
<b>Figure 4.4</b> Simulated and measured return loss of the designed antenna .....	43
<b>Figure 4.5</b> Simulated and measured VSWR of the designed antenna .....	44
<b>Figure 4.6</b> Simulated peak gain plot as a function of frequency.....	44
<b>Figure 4.7.</b> Simulated radiation efficiency plot as a function of frequency.....	45
<b>Figure 4.8.</b> Radiation pattern of the antenna at 5.2 GHz for a) $\varphi = 0^\circ$ and b) $\varphi = 90^\circ$ planes .....	46
<b>Figure 4.9.</b> Radiation pattern of the antenna at 10.8 GHz for a) $\varphi = 0^\circ$ and b) $\varphi = 90^\circ$ planes ...	46

<b>Figure 4.10.</b> Radiation pattern of the antenna at 28.5 GHz for a) $\varphi = 0^\circ$ and b) $\varphi = 90^\circ$ planes .	47
<b>Figure 4.11.</b> 3D Simulated radiation pattern of the designed antenna at (a) 5.2 GHz, (b) 10.8 GHz, and (c) 28.5 GHz frequency.....	47
<b>Figure 5.1.</b> Proposed 5G modified bow-tie antenna architecture, (a) top layer and (b) bottom layer .....	51
<b>Figure 5.2.</b> Simulated return loss results of the 5G modified bow-tie antenna as a function of frequency.....	53
<b>Figure 5.3.</b> Simulated return loss results of the 5G modified bow-tie antenna as a function of frequency.....	53
<b>Figure 5.4.</b> Simulated H-field distribution at 18.35 GHz frequency.....	54
<b>Figure 5.5.</b> Simulated H-field distribution at 18.35 GHz frequency.....	54
<b>Figure 5.6.</b> Simulated radiation pattern of the antenna at 18.35 GHz frequency for, (a) $\Phi=0$ and (b) $\Phi=90$ planes .....	55
<b>Figure 5.7.</b> 3D simulated gain pattern of the proposed 5G antenna.....	55
<b>Figure 5.8.</b> Geometry of the phased array antenna, (a) Top View, two elements array, (b) Bottom View, two elements array, (c) Top View, four elements array, (d) Bottom View, four elements array, (e) Top View, eight elements array, (f) Bottom View, eight elements .....	56
<b>Figure 5.9.</b> S21 characteristics of the eight element antenna for different values of d.....	57
<b>Figure 5.10.</b> Simulated S parameters of proposed eight element antenna .....	58

**Figure 5.11.** 2D radiation pattern and 3D gain of the proposed eight element array antenna at different positive scanning angles ( $0^{\circ}$ ,  $15^{\circ}$ ,  $30^{\circ}$ ,  $45^{\circ}$ ,  $60^{\circ}$ ,  $75^{\circ}$ )..... 59

**Figure 5.12.** 2D radiation pattern and 3D gain of the proposed eight element array antenna at different positive scanning angles ( $0^{\circ}$ ,  $-15^{\circ}$ ,  $-30^{\circ}$ ,  $-45^{\circ}$ ,  $-60^{\circ}$ ,  $-75^{\circ}$ ). ..... 60

**Figure 5.13.** Simulated 2D radiation beams of the proposed antenna at 18.35 GHz frequency with different scan angles ..... 61

## Dedication

Dedicated to all underprivileged street children in the world

## CHAPTER 1: INTRODUCTION

### 1.1 Background

With the growing research and development of ubiquitous wireless technology, our everyday life is becoming covered with wireless devices. These devices embed with the electronics, sensors, actuators, and software can exchange the data and information, are what is called The Internet of Things (IoT). IoT has numerous applications: wearables, healthcare, smart skins, functional clothing, mobile network/internet devices, and to name a few [1].

Since many of the applications are directly or indirectly involved with the flexible electronic products, the fabrication of flexible electronics is of great interest to the researchers because of its rapidly expanding market which is expected to reach \$200 billion by the next ten years [2]. These electronic products can be manufactured adopting inkjet printing technology, a straightforward and cost-effective method to fabricate electronic devices on flexible substrates [3-7], unlike photolithography.

Further, the evergrowing IoT applications demand connectivity among devices, such as a device to human, device to device, machine to machine, system to system, and so on [8]. In order to establish the connection over multiple devices, it demands connectivity over multiple bands, whereas the conventional systems allocate a distinct frequency range for the individual band [9]. So, to adopt IoT systems using existing technology, each system may require many antennas with variable sizes, which could be a challenging task to deploy all into a small device. Ultra wide-band (UWB) technology can replace all single narrowband antennas with a unique design to tackle the mentioned difficulties [10].

As the main motive is to ensure connectivity of as many as possible devices with a higher network speed, the next generation (5G) technology with frequency band ranging from 10 GHz to 80 GHz is required to secure a reliable ubiquitous connectivity and diversity of data [11]. However, with the increase of operating frequencies would bring new challenges to design and implement the antennas [12].

Sections 1.2 of this chapter presents a review of inkjet printing methods. Sections 1.3 illustrates detailed quick reviews and performances of ultra-wideband antennas (UWB) on both flexible and rigid substrates. The need for millimeter wave (mmWave) antennas and the potential of 5G technology as a possible candidate to overcome traffic and network speed issues are discussed in section 1.4. An outline of the motivation and research goals of the thesis is given in Section 1.5. Finally, section 1.6 presents an organizational roadmap of the thesis.

## **1.2 Inkjet printing**

Inkjet printing is a fast and advanced technology which utilizes conductive ink to fabricate devices without iterations in photolithographic mask design or etching methods. Hence, the process is controlled by the user's computer program and does not necessarily require a clean room environment [13]. It is a horizontal bar-by-bar printing technique employing a cartridge which comprises of a Piezo-driven jetting device with an integrated reservoir and heater. The volume of the droplet decides the resolution of the printer. The details of the inkjet printer used for this thesis is shown in Fig. 1.1. Silver nano-particles ink are usually considered in the inkjet printing process to satisfy metal conductivity over the paper substrate, an environmentally friendly material that can set the foundation for the green RF electronics, devices, and modules [14].

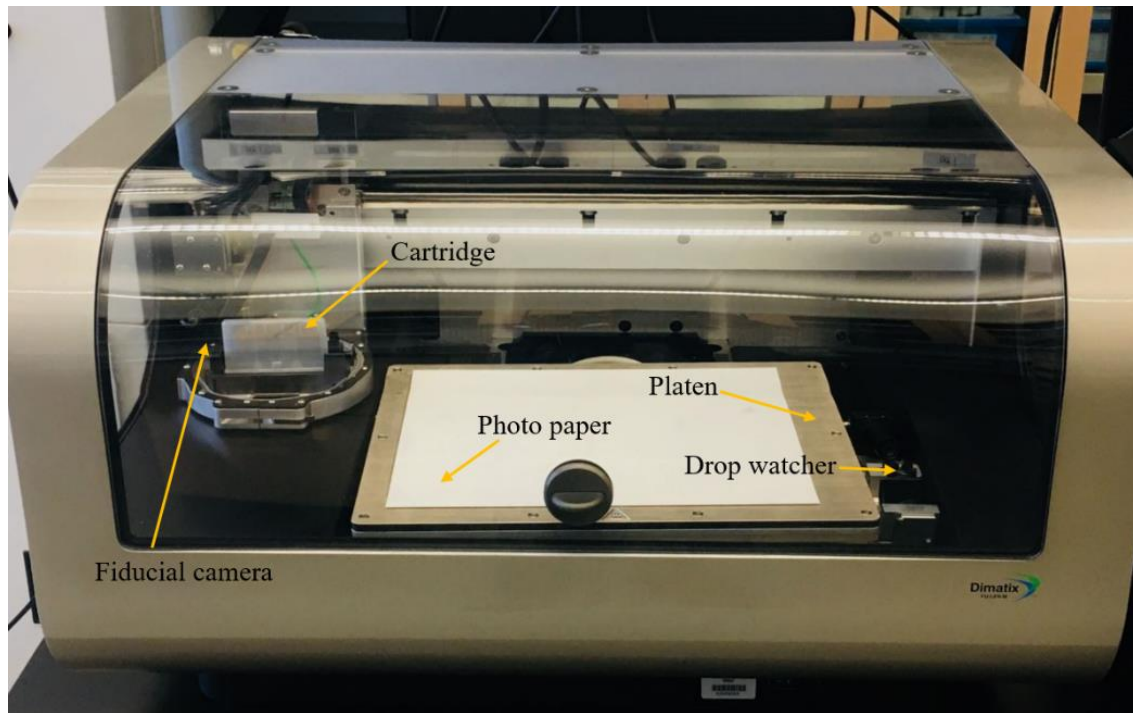


**Figure 1.1.** Details of the Fujifilm's Dimatix Inkjet Printer, DMP 2831

### **1.3 Ultra wideband (UWB) antennas**

Ultra-wideband generally refers to signals or systems that have a large relative bandwidth which will overlap with the existing narrowband wireless signal or systems. It is widely used in a wide range of frequency applications including radar, medical imaging, collision detection, military applications, wearables, autonomous cars, vehicle radar systems, intrusion detection, UWB tags, and to name a few. UWB systems have satisfied by Federal Communications Commission (FCC), and there are several advantages to use this technology over others. However, the main benefits are robust characteristics to the multipath environment, extremely degree of freedom to interfere other signals, and a broad frequency spectrum at a shallow power level which is comparable to the noise floor level. Also, in many cases according to the application, many single narrow-banded antennas can be replaceable with a single UWB antenna because of its high

performance in multipath channels. Another good thing about UWB technology is to adaptability with the rigid and flexible substrates for both flexible or wearable and multiservice communications. The operational behaviors of the UWB signal over others can be illustrated in Fig. 1.2.

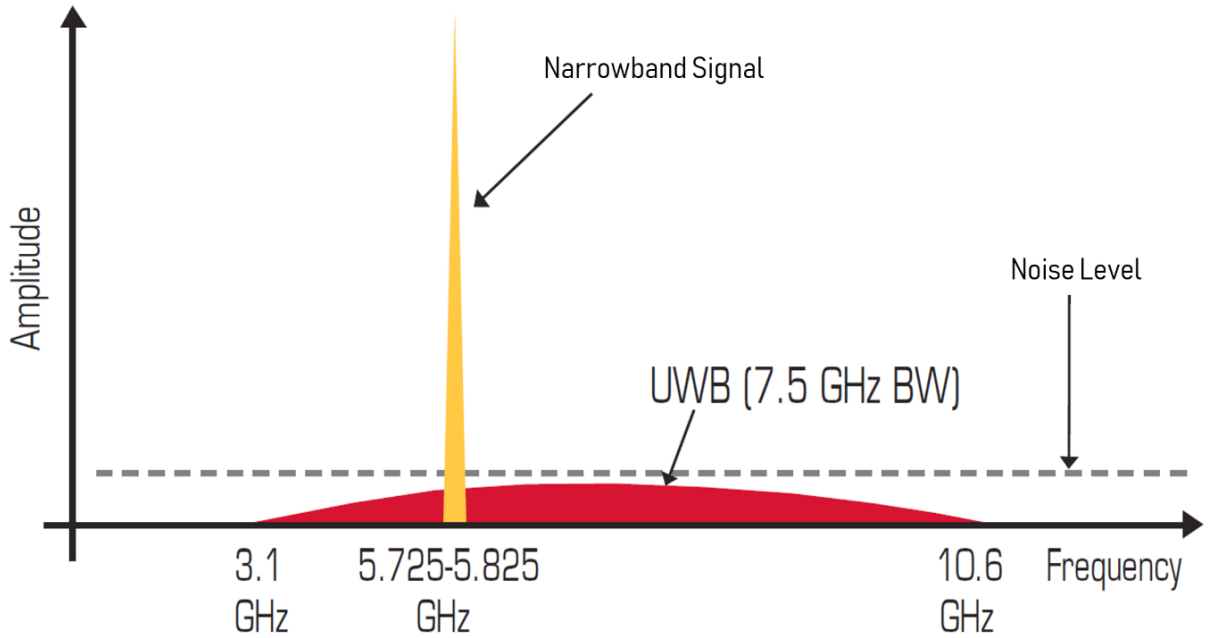


**Figure 1.2.** Spectrum of UWB signal compared with narrowband Signal [15]

#### 1.4 5G Antenna

The demand for high-speed data and the need for more spectrum have pushed the use of 5G technology and millimeter-wave (mmWave) frequencies for future IoT and wireless devices. The 5G antennas have been attracting significant attention because of the availability of the multiple operating bands [16]. The term IoT and 5G are used conversely because of their shared traits. The main difference of 5G technology with 4G or others is to use the beam steering array antenna where an individual element covers the frequency spectrum with higher signal strength.

On the conversely, the traditional methods use Omnidirectional antennas with moderate gain [17]. The number of the array elements and the placements of the elements can be varied concerning the operating frequency range, gain, types of wireless devices or applications. Due to the small wavelength, 5G or mmWave antenna size is also smaller than the conventional design that enables to extract the sharp beamforming technology.

## **1.5 Motivation and Research Goals**

In this chapter, we have provided an overview of the emerging antenna technology for the IoT, wearable, and 5G networks. There are two different types of challenges for flexible and rigid antennas associated with the IoT based wireless devices. The challenges associated with flexible antennas such as the conductive performance of the printed specimens, surface roughness, ink depositions, flexible or reconfigurable behaviors in harsh conditions are discussed. We have emphasized that inkjet printing properties in flexible antenna fabrication have become more of a concern and it is a general challenge to all printing electronics which reduces conductivity, increases operating costs, fails to operate in harsh conditions. Most of the previous studies related to flexible sensors and antennas are given more priority on their design (sensors, antennas) instead of establishing an ideal printing condition for a particular substrate and ink. Although such approaches should have the highest priority to improve this field in many ways especially considering cost and time optimization, conductive performance. On the other hand, for the 5G antennas with the rigid substrate, the main challenge is to design an antenna with the greater bandwidth. We have given more emphasized to improve the bandwidth which can accommodate high traffic and increase the communication network speed by varying the antenna architecture. The major goals and contributions of this thesis work are outlined as follows.

- In order to bridge the gap between inkjet-printed circuits or device manufacturers and designers, optimized inkjet printing properties for a set of materials (photo paper, and silver nanoparticles ink) have been established after a lot of experimental iterations and statistical data analysis.
- Design an efficient IoT or wearable ultra-wide-band (UWB) antenna and fabricated one design utilizing our own developed investigated properties in order to take real measurements of its performance. Analysis and investigation of the impact of bending characteristics on resistivity results.
- Design a relatively similar UWB antenna on a rigid substrate and see how it works differently or affects antenna's electromagnetic behavior.
- Propose a new model in order to keep pace with the growing research and development on next-generation 5G wireless networks. In this regard, an antenna is designed and optimized to analysis the key 5G antenna parameters, such as bandwidth, mutual coupling, scanning properties, and radiation pattern.
- Analyze the results for every experiments and summarizes the outcomes.

## **1.6 Thesis Organization**

The current chapter gives a brief introduction to the growth of IoT, wearable, and 5G antenna technology and its capabilities while listing some challenges that could potentially hinder practical implementations and applications.

The subsequent sections of this thesis are organized in chapters with the following content:

Chapter 2 reviews the importance of employing inkjet printing technology as a fast and straightforward fabrication technique with silver nanoparticles ink. It also highlights the benefits

of using paper as a substrate for versatile applications. As such, the possibility of microwave frequency applications, reel-to-reel, and multilayer printing capability, and compatibility with inkjet printing. It discusses in detail the methodologies and approaches used for inkjet printing and different printing parameter variations. The impact of these systematic and random variations was explored and surveyed how they propagate and affect the performance of printed patterns. The need for a new investigation of inkjet printing properties on the paper substrate including statistical analysis was experimented to overcome the effects of those process variations and their impact on printing electronics.

Chapter 3 focusses on flexible antenna design employing inkjet printing technology and silver nanoparticles ink on Kodak photo paper. Our developed optimized printing conditions were utilized to print the antenna on the paper. This chapter discusses an ultra wide-band (UWB) monopole antenna design, simulation, and experimentations, which operates over 3.2-30 GHz frequency spectrum. The simulation and experimental results are presented, which compliances with the Federal Communication Commissions' (FCC) UWB requirements and flexible characteristics of the IoT or wearable products.

Chapter 4 presents another UWB monopole antenna on the rigid, FR4 substrate, ranges over a 4.0-40 GHz. Based on the simulation and experimental results this chapter highlights how this microstrip feed design can be used in six different bands and multiservice wireless communications.

In chapter 5, a new and modified bow-tie wideband (3 GHz bandwidth) microstrip 5G antenna have been designed, investigated, and simulated. This includes design details of the single element antenna as well as two or more element based phased array 5G antennas. It presents how

gain values of the array antenna can be increased based on the system requirement or applications after increasing the number of array elements. Finally, the results in terms of return loss, bandwidth, impedance matching, mutual coupling, gain, radiation pattern, and beam steering characteristics are presented.

Chapter 6 concludes the thesis by explaining the importance of this research and highlights the critical next steps towards the adaptabilities of the designed antennas for environmentally friendly IoT, wearable, and 5G applications.

## CHAPTER 2: INVESTIGATION OF PRINTING PROPERTIES ON PAPER SUBSTRATE

### 2.1 Background

Recent advancements in printed electronics have enabled the development of flexible devices and IoT products [18], antenna [19], sensors [20], solar cells [5], organic resistor [21], organic transponder [22], flexible battery [23] to name a few. The field of flexible devices and wearables is growing fast primarily due to its eco-friendly and cost-effective fabrication methodologies.

Modern inkjet printing is advanced which utilizes conductive ink to fabricate devices without iterations in photolithographic mask design or etching methods [24]. Inkjet printing can be performed employing any conductive, resistive, and biological inks, with wide varieties of substrates including paper, PET film, textiles, fibers, etc. The electrical and mechanical properties of the printed samples depend on the type and quality of ink, as well as the surface characteristics of the substrate. Fujifilm's commercially available Dimatix 2831 printer has been frequently used to print patterns on different substrates under various printing conditions [25]. The paper-based substrate has become popular to realize devices due to its versatile used and properties that include the possibility of microwave frequency applications, reel-to-reel printing capability, low cost in nature, availability of hydrophobic or fire retardant type, low surface profile, multilayer printing options, and compatible with inkjet printing [26]. The hydrophobic and resin coated, Kodak photo paper is a common choice due to its conductive single layer traces allowing multiple layers of printing capability [27]. There are numerous research papers regarding inks, where many researchers have claimed to have founded excellent device performance using either gold [28] or

copper [29] ink. However, when devices are implemented utilizing such inks, they quickly convert into their oxidized form ( $\text{Au}_2\text{O}_3$  or  $\text{CuO}$ ) rendering them insulating. In addition, the required curing temperatures of gold and copper exceed the temperature that the paper substrate can withstand. Silver nanoparticle ink (AgNP) is preferred over Au or Cu due to its lower melting temperature [30], lower cost [31], minimal resistance to corrosion [27], and low reactivity in the air [32]. Apart from the ink, the critical factor that influences the conductivity of the printed samples is sintering. The sintering process can dry out the ink swiftly and remove the bubbles[33, 34]. The sintering temperature needs to be carefully chosen as over-sinter or under-sintering can break the printed lines and degrade the overall quality of printed devices.

In this context, this chapter reports on optimum printing parameters when using silver nanoparticle ink to print patterns on Kodak 4-Star photo paper substrate. The Compound Microscope, Scanning Electron Microscope (SEM), Optical Profilometer, multimeter and four-point probe were used to inspect the samples for surface roughness and conductivity.

## **2.2 Experimental**

### **2.2.1 Printing**

The printer used for this project was the Fujifilm's Dimatix 2831 Inkjet Printer. The DMP printer offers drop-on-demand (DOD) piezoelectric ink-jet nozzles to ensure precision drop placement. It uses 10 pL drop-size cartridges (model: DMC-11610) for this experiment, which hold 1.5 mL of ink. During filling of the cartridge, it is prescribed by the manufacturer to avoid air, and keep the cartridge minimum 30 minutes in the idle state. It is recommended the cartridge be loaded in the printer carriage during this time, before giving the printing command [35].

The ink used in this experiment was Ag Nanoparticle Inkjet 9104 Ink, purchased from Methode Electronics. The viscosity, density, and surface energy are as follows: 9 cps, 1.3 g/ml, 33 dynes/cm respectively. These ink properties ensure  $25 \text{ m}\Omega/\square$  is the printing electrical resistance. The optimum fluid physical characteristics include a viscosity of 10-12 cps and a surface tension of 28–36 dynes/cm [25]. Patterns sampled were first created using the ANSYS EM simulation software, and saved as a .DXF file, which then were converted to a bitmap file through the ACE3000 V7 software, and finally uploaded to the Dimatix program. Using the bitmap file uploader on the DMP, the resolution, drop spacing, layers, leader bar width, and reference point were set. A leader bar was used by printing a vertical line to the left of the pattern, to pre-jet nozzles and keep their drop velocity uniform.

**Table 2.1** Optimal printing parameters

Jetting Voltage	13.5 V
Jetting Frequency	4.5 kHz
Drop Size	10 pL
Drop Spacing	15 $\mu\text{m}$
Layers	2
Printing Print Height	750 $\mu\text{m}$
Cartridge Temperature	38° C
Platen Temperature	30° C

To find the optimum printing technique, the drop spacing was varied from 5  $\mu\text{m}$  to 20  $\mu\text{m}$ . If the drop spacing is too close, it causes excess ink to form uneven lines in the print, resulting in poor print quality and conductivity. In contrast, too far of a drop spacing results in broken connections in the drops being ejected. Through visual inspection, the optimum drop spacing resulting in uniform print lines was found to be 15  $\mu\text{m}$ . The optimal printing parameters for this research are given in Table 2.1. Fig. 2.1 illustrates the working principle of inkjet printing.

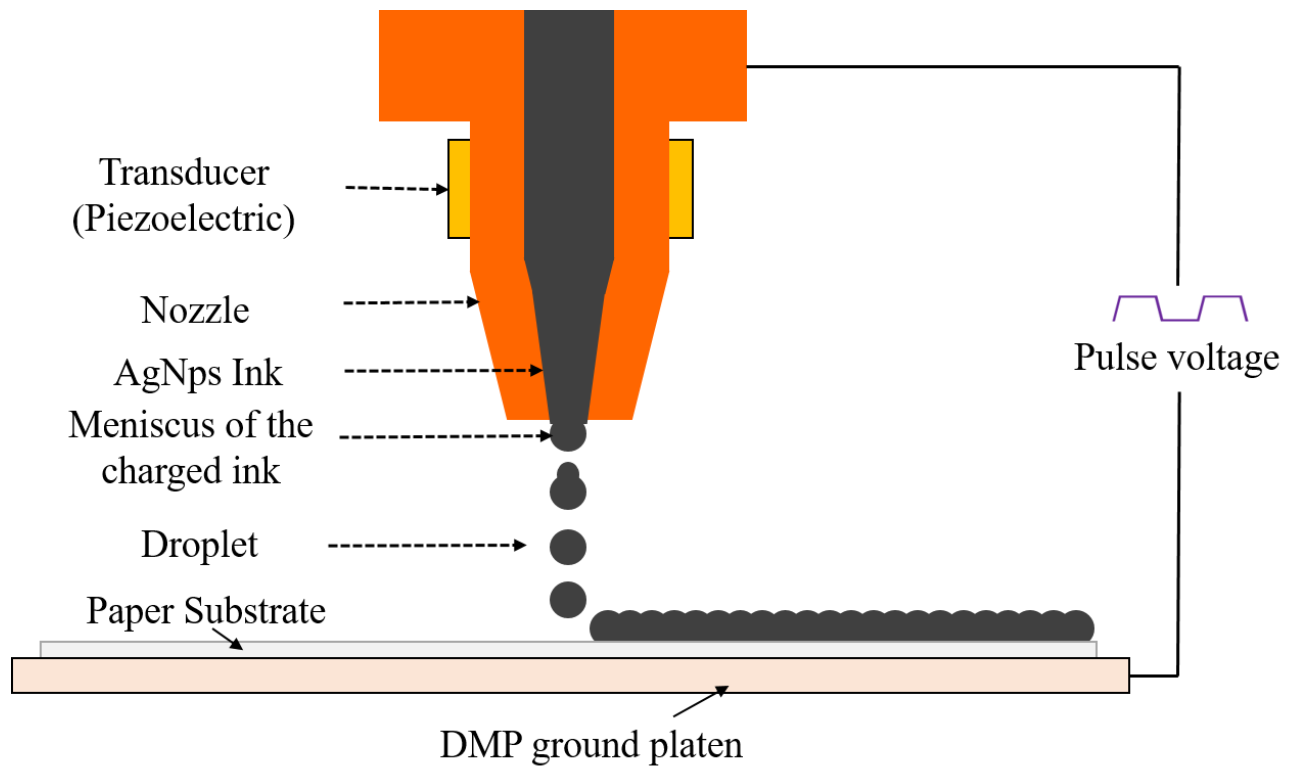


**Figure 2.1.** Inkjet printing process

After waiting at least 30 minutes, the Drop Manager software was used to inspect the drop quality for the Ag nanoparticle ink. The key is to create uniform drops, falling with matching drop velocity, without a tail or any satellite drops lagging behind, to be formed in sequential jets. The DMP requires the jets chosen for printing to be sequential, and for this reason, four subsequent

uniform drop-jets were chosen. To inspect the printed pattern, and to set the printing origin, the printer utilizes the Fiducial Camera, which has a resolution of  $2.54 \mu\text{m}/\text{pixel}$ . Drop spacing is varied by adjusting the cartridge angle. The Fiducial Camera is also used to do a drop offset, consisting of a 10 mm line in the X direction and a single dot 1 mm next to the line.

Cleaning cycle is another important setting which helps to avoid jets clogging and ink settlings. Cleaning cycle settings include three functions: purge, spit, and blot. After filling a new cartridge, it is important to run a cleaning cycle with purge, pushing air and debris out, clearing the nozzles. In this experiment, while printing, the group used a cleaning cycle consisting of the blot, using a non-contact absorption pad, every 6 lines to maintain a clean print head. Once successfully printed, the samples were inspected via the DMP's Fiducial Camera. A sample printed pattern is shown in Fig. 2.2.

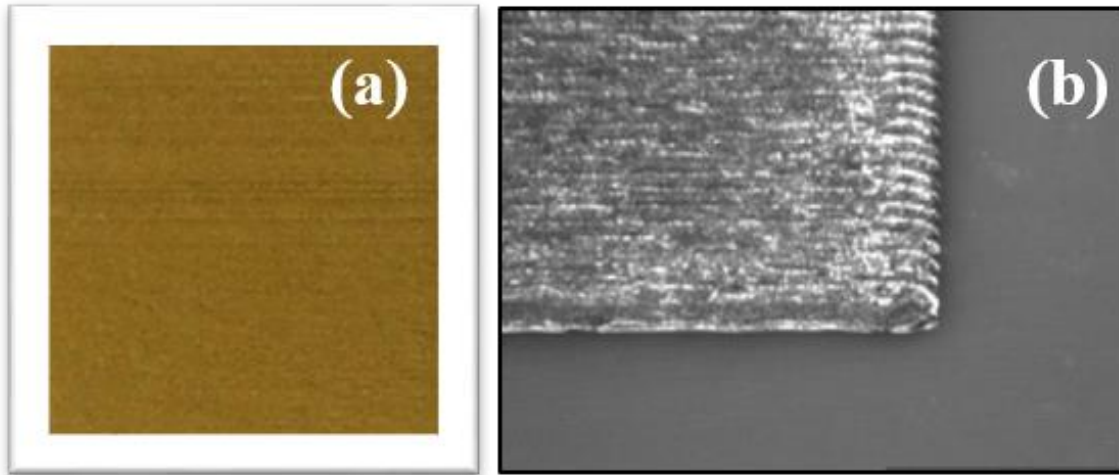


**Figure 2.2.** Image of the sample printed pattern acquired with a) digital camera, b) Fiducial Camera of DMP.

### 2.2.2 Sintering (Heat Treatment)

Among various types of sintering techniques, the most straightforward method is thermal sintering. The experiment was conducted using Thermo Fisher Scientific's digital hot plate (Model: HP88857100). Silver nanoparticles fuse at a much lower temperature than bulk Ag. If  $T_{\text{melt}}$  is the melting point of metal nanoparticles,  $T_{\text{bulk}}$  is the melting point of solid metal,  $\sigma$  is the characteristic parameter, and  $R$  is the radius of metal particles. Then, the relationship among these variables is given below [36].

$$T_{\text{melt}}(R) = T_{\text{bulk}} \left( 1 - \frac{\sigma}{R} \right) \quad (1)$$

Based on equation (1) and the limitation of the paper substrate, the printed layers (single, double and triple) were cured at 60 °C, 75 °C, 90 °C, and 120 °C for 30 minutes. The conductivity of the printed patterns was evaluated and compared with plain air drying.

### 2.2.3 Resistivity Measurements

Electrical resistivity describes appropriate signal carrying capability of a conducting path. It depends not only upon the chemical properties of the silver nanoparticles, but also the geometry of the printed pattern: length ( $L$ ), width ( $W$ ), and thickness ( $t$ ). Resistivity is given by[37]:

$$\rho = R \frac{A}{L} = R \frac{W \times t}{L}, (\Omega \cdot \text{cm}) \quad (2)$$

To quantify the resistivity of the pattern, the resistance of the sample was measured employing two-point probe (Fluke 87 V industrial multimeter) and the results verified with Jandel's four-point probe. Then, the thickness of the layer was measured using both a Scanning

Electron Microscope (Quanta 3D 200i) [38] and Optical Profiling System (Veeco WYKO NT 1100) [39].

#### **2.2.4 Flexibility Test**

Mechanical reliability has been a primary limiting factor towards realizing a vast array of flexible devices. To test the effect of bending, an earlier study [40] conducted several bending tests, using the varied diameter of cylindrically shaped pattern, and deformed it using their hands. A similar approach was followed in this article, and the resistivity was evaluated (as a function of bending) and compared with the resistivity of previously recorded non-bended results.

#### **2.2.5 Surface Roughness Measurement and Surface Characterization**

The sharpness of the edges, smoothness of the printing, and ink distribution were checked using the Fiducial Camera of DMP and CD microscope (Nikon MM-400). Surface roughness was measured using the Optical Profiling System [41]. On the other hand, SEM (Quanta 3D 200i) [42] was used to investigate the thickness of the layer and surface morphology.

### **2.3 Results and Discussion**

#### **2.3.1 Sintering and Resistivity Results**

The resistivity of the printed pattern as a function of sintering temperature is shown in Table 2.2. The resistivity of air-dried patterns was exceptionally high due to the printed particles forming porous thin films over another porous paper substrate. The measured resistivity gradually decreased with an increase in sintering temperature. A change of color of the printed pattern from yellowish-brown to tan was observed with increasing sintering temperature. Further, 15  $\mu\text{m}$  drop spacing provided higher conductivity results than compared to 10  $\mu\text{m}$  drop spacing.

**Table 2.2** Resistivity results at different curing conditions and drop spacing

Sl. No.	Sintering Temperature (°C)	Cooling Period min	Resistivity * 10 <sup>-4</sup> Ω-cm					
			Single Layer		Double Layer		Triple Layer	
			10 ds	15 ds	10 ds	15 ds	10 ds	15 ds
1	Air	720	11800	2880	8300	1300	9580	970
2	60	30	84.87	26.32	37.1	19.8	29.9	7.86
3	75	30	21.71	6.8	3.6	5.4	3.24	2.62
4	90	30	1.13	0.283	0.54	0.18	0.262	0.262
5	120	30	0.47	0.189	0.18	0.18	0.262	0.262

Firstly, to figure out an optimum drop spacing, this experiment considered many from 5 μm to 20 μm and the above table compared the data for 10 μm, and 15 μm drop spacing respectively. Irrespective of the number of printed layers, the resistivity of the patterns plummeted after curing. Theoretically, the triple layer should have the highest conductivity. However, the double layer resistivity is lower compared to the triple layer at 120 °C. Such an anomaly might be speculated due to the possibility of miniscule cracks and discontinuities of ink explored further in this article. The resistivity versus temperature curve is given in Fig. 2.3, which shows the drastic fall of resistivity of printed samples for sintering temperatures above 60 °C. The best conductivity was found for double layer printed samples cured at 90 °C, (resistivity: 1.8 x10<sup>-5</sup> Ω-cm, and conductivity: 5.56 x 10<sup>6</sup> Ω<sup>-1</sup>m<sup>-1</sup>).

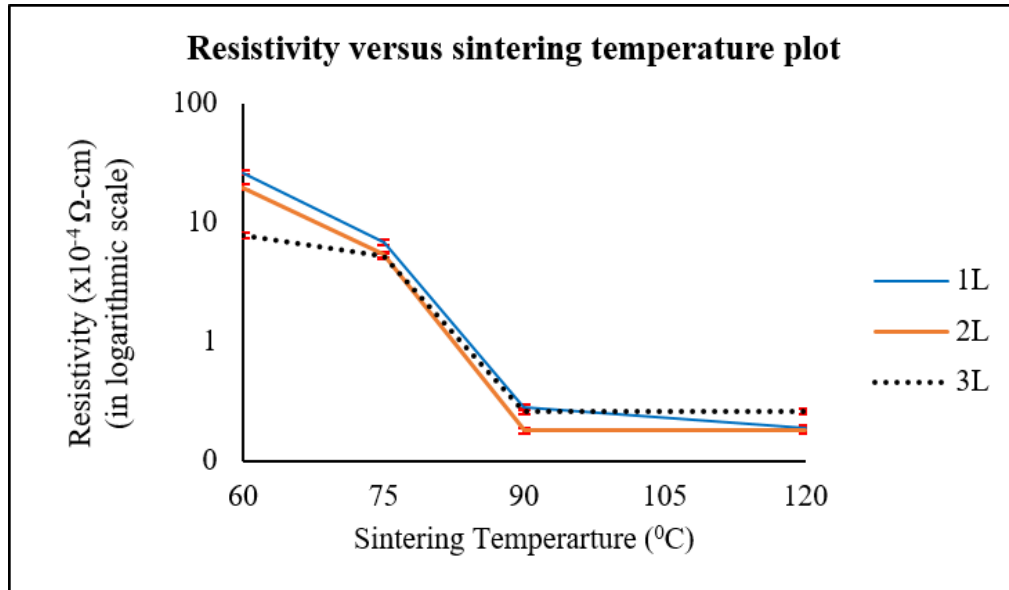


**Figure 2.3.** Resistivity result of samples with different curing temperatures. The error bar represents standard deviation. (Number of printed layers, 1L: One layer, 2L: Two Layer, and 3L: Three Layer)

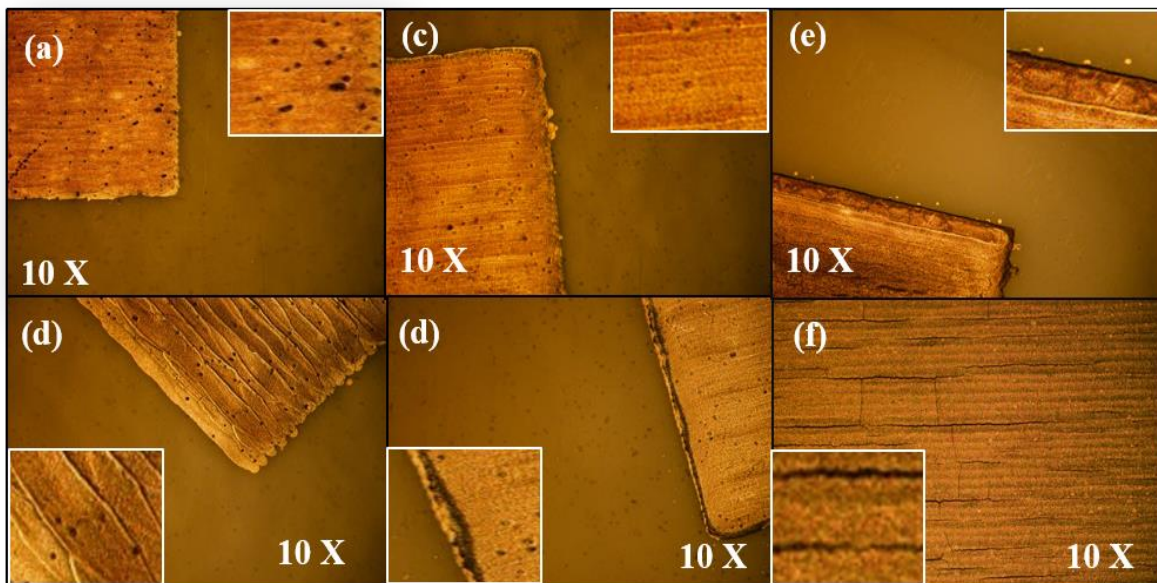
The resistivity values after 90° were almost the same for all printing thicknesses. To analyze the significance of sintering temperature on pattern resistivity, one-way analysis of variance (ANOVA) analysis was pursued. The ANOVA results (Table 2.3) indicate with a level of significance ( $\alpha=0.05$ ) that the sintering temperature is a significant factor affecting resistivity.

**Table 2.3** ANOVA Analysis

Source	SS	DF	MS	F <sub>0</sub>	F <sub>critical</sub>	P-Values
Sintering Temperature	6.316E-06	3	2.1E-06	9.528	4.066	p<0.05
Error	1.768E-06	8	2.2E-07			
Total	8.084E-06	11				

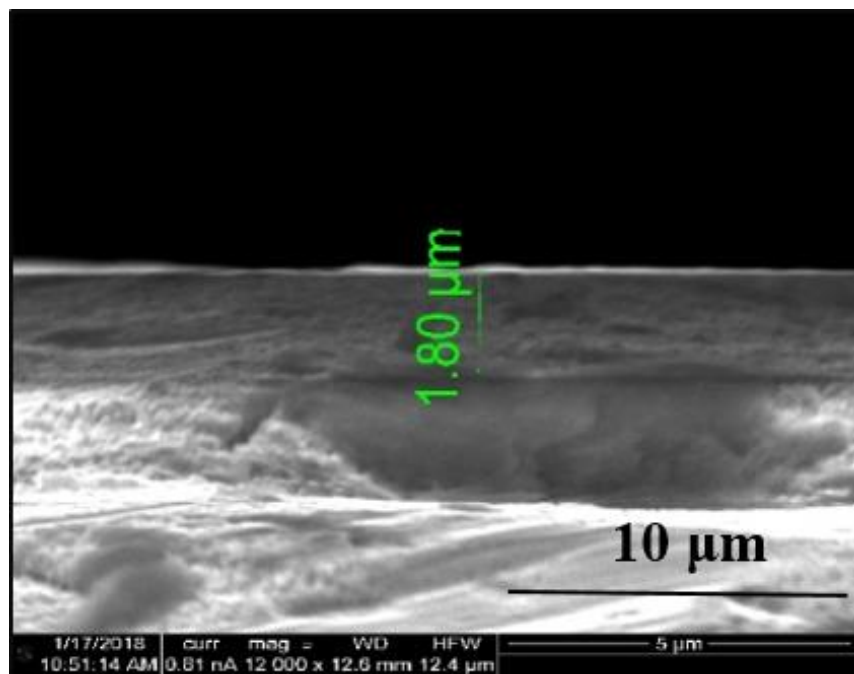
### 2.3.2 Surface Characterization

Imaging the corner side of the printed patterns was a priority as these are the most failure-prone areas after printing [21]. Figure 2.4 presents CD microscopy images of three different layers of printed samples. Images were taken at 10x magnification. Fig. 2.4(a) and 2.4(b) shows the single layer printed pattern cured at open air and 90 °C respectively. A lot of pinholes, as well as non-continuous printed lines, can be seen before curing. After curing at 90 °C, the edge quality improved and brought ink closer. Yet, the pattern contained many holes. The size of the hole of the substrates overtime may increase, decreasing the conductivity and eventually deteriorating the performances of the devices.



**Figure 2.4.** CD microscopy images to observe ink deposition, holes, crack, and coffee ring effect at 10X magnification level. The printed samples are: (a) single layer, air cure, (b) single layer, cured at 90 °C, (c) double layer, air cure, (d) double layer, cured at 90 °C, (e) triple layer, air cure, and (f) triple layer, cured at 120 °C.

Fig. 2.4(c) and 2.4(d) shows the images for double layer printed pattern. A significant improvement in printing quality has been observed: sharp edges, uniform ink depositions, fewer holes, and increased bonding with the substrate. A closer observation of the image reveals coffee stain effects, particularly after curing. This effect can be controlled by decreasing the voltage of the droplets further in the cartridge settings. For the three layer printed pattern (Fig. 2.4(e)) which is air cured, there are relatively no holes, ink is distributed evenly. But, there seem to be some satellite spots, which were not present for the single and double layer prints. When cured to 90 °C and above, miniscule cracks appeared to form. At 120 °C, there were even more cracks present (Fig. 2.4(f)). The probable cause is speculated to be that the increased amount of silver nanoparticles, as well as the associated impurities disintegrate at higher sintering temperatures. However, for single or double layers of printed patterns, such cracks or fatigues were absent.



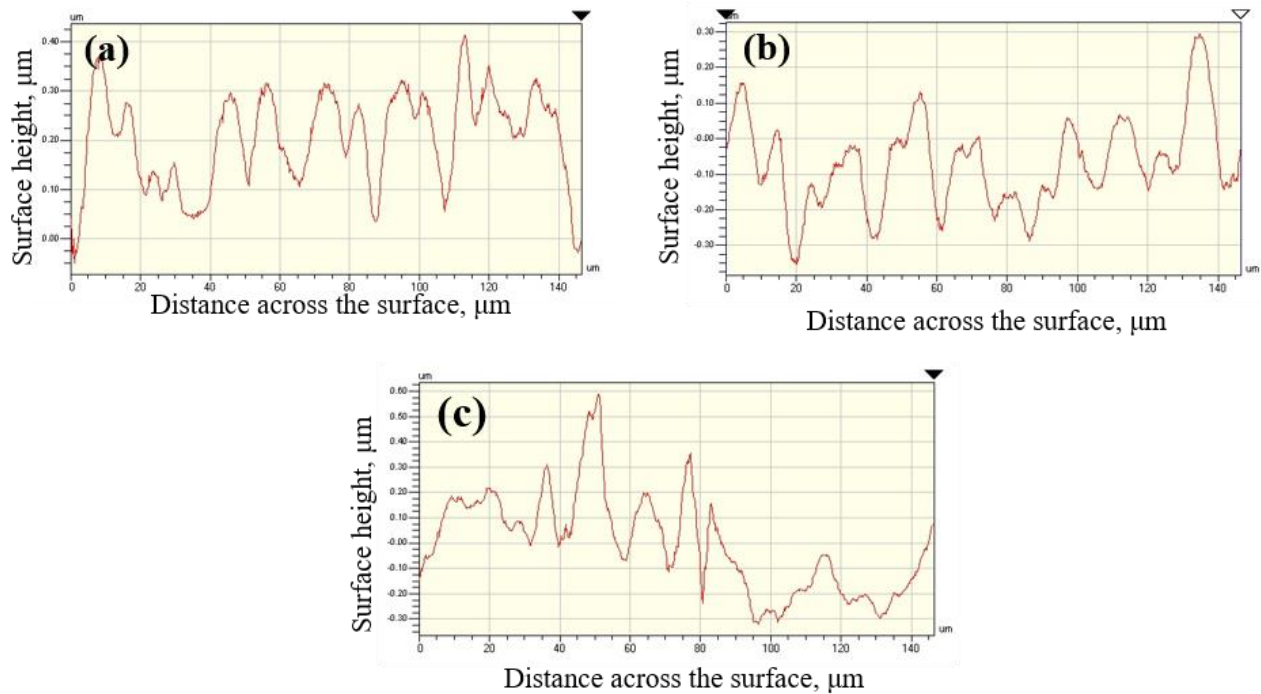
**Figure 2.5.** Thickness of double-layer printed samples using SEM.

Figure 2.5 shows the thickness of the double layer printed samples cured at 90 °C for 30 minutes utilizing 15 drop spacing. The thickness of the double layer printed pattern was found to be 1.8 μm.

**Table 2.4** Layer thickness of the printed patterns

Layer	Single	Double	Triple
Thickness, (μm)	0.944	1.8	2.62

Table 2.4 shows the thickness of single, double, and triple layer printed patterns cured at 90 °C. As expected, the thickness increased with an increase in layer thickness.



**Figure 2.6.** Surface roughness analysis using the Optical Profiler of (a) Single layer, (b) Double layer, and (c) Triple layer printed samples.

The 2D surface topographies of printed samples with different layer thickness cured at 90 °C is shown in Fig. 2.6. These graphs were obtained using the Veeco software associated with the Optical Profiler. The average roughness values of the different printed samples were calculated using MATLAB. Table 2.5 shows the surface roughness values as a function of the number of layers of printed pattern. This table indicates that the increase of the number of layers of printed pattern increased the average surface roughness, but not proportionally.

**Table 2.5** Average roughness of 3 different printed layer samples

Layer	Single	Double	Triple
Roughness, (nm)	289	328	356

SEM micrographs of the surface of the different printed layers are shown in figure 2.7. Figures 2.7(a), 2.7(b), and 2.7(c) are the SEM pictures of the single layer, double layer, and triple layers of printed patterns respectively, cured at 90 °C for 30 minutes. The number density of holes seems to decrease gradually from Fig. 2.7(a) to 2.7(c). Due to the cracking and pinhole issues in triple and single layer printing patterns observed earlier, we had chosen to focus on double-layer pattern for further analysis. The double layer pattern seems to deliver the best printing results of this particular substrate. It also cuts down one-third of the cost of printing (ink, cartridge, cleaning pad, drop watcher pads, etc.) related to material consumption compared to three-layer printed pattern. According to Fig. 2.7(d), 2.7(e), and 2.7(f), smooth surface morphology is observed for the double layer printed patterns at different sintering temperatures. The silver nanoparticles appeared to have fused which helped boost up the conductivity upon sintering at different temperatures.

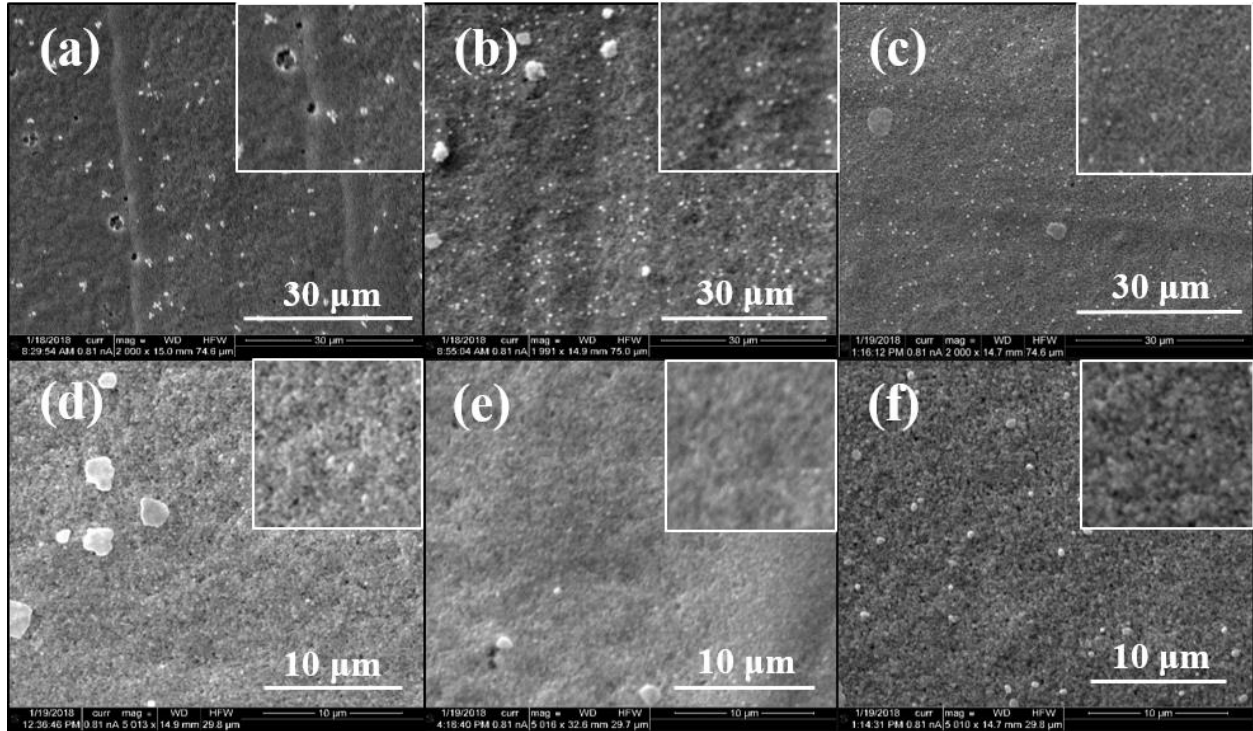


**Figure 2.7.** SEM pictures for microstructural variations on the pattern surface as a function of number of printed layers and sintering temperature. The effect of amount of layer printed and cured at 90 °C for a (a) single layer, (b) double layer, and (c) triple layer sample. Surface morphology of double layer printed pattern sintered at (d) 60 °C, (e) 90 °C, and (f) 120 °C.

Mechanically induced electrical degradation is a primary concern for flexible devices. To test such an effect, bending tests were conducted for single and double layered printed samples using two different sizes of cylindrical shaped structures (12mm and 18 mm diameter), over which patterns were rolled [40]. In addition, specimens were bent using hand fingers differently. Fig. 2.8(a) and Fig. 2.8(b) shows the bending test. A quick test of the resistivity of the samples before and after bending indicated a  $\pm 0.5\%$  change implying the printed patterns were robust even after subjecting to mechanical bending stress.

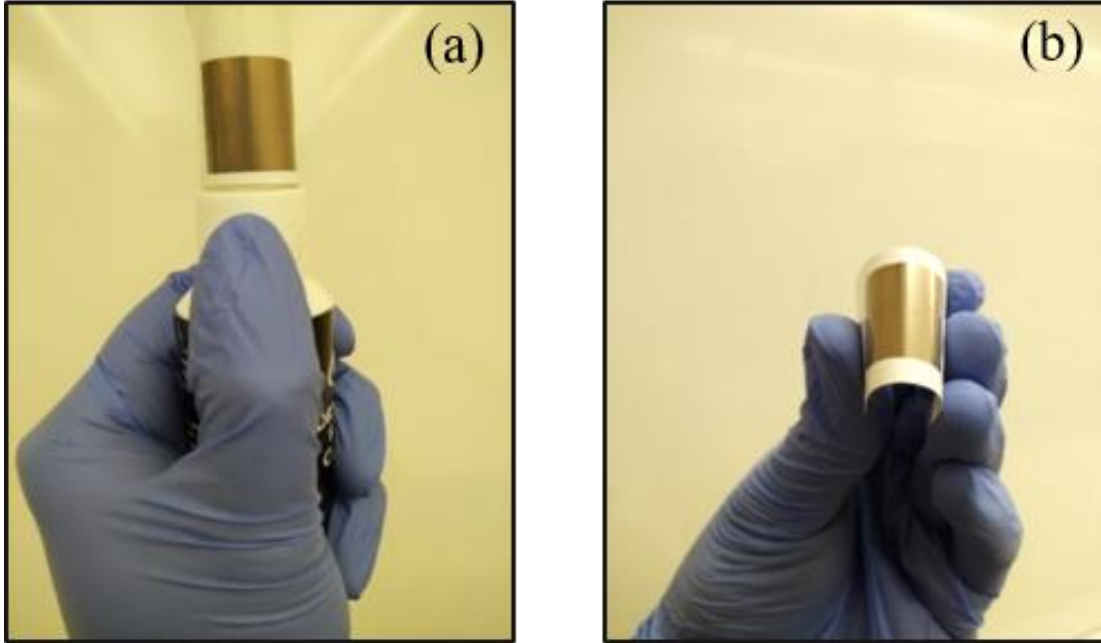


**Figure 2.8.** Bending test using (a) cylindrical shape structure and (b) hand.

## 2.4 Summary

In this chapter, the electrical property and surface morphology of different layers of ink-jet printed patterns on the paper substrate were investigated as a function of sintering temperature. ANOVA analysis indicated that the sintering temperature is a significant factor affecting conductivity of the samples. Among the three printed layers, the double layer printed pattern (cured at 90°C for 30 minutes) exhibited superior conductivity (conductivity:  $5.56 \times 10^6 \Omega^{-1}\text{m}^{-1}$ ) along with a smooth morphology. Repeated bending tests did not change the electrical resistivity significantly indicating the durability of the double layer printed pattern. The results from this investigation will enable the development of a wide variety of paper-based devices for IoT applications.

## CHAPTER 3: A CPW-Fed Flexible UWB Antenna for IoT Applications

### 3.1 Background

Wireless devices on flexible substrates play a critical role in numerous IoT applications including wearables, healthcare, smart skins, functional clothing, and mobile network/internet devices to name a few [1]. The IoT applications demand connectivity among devices over multiple frequency bands, whereas conventional systems allocate a distinct frequency range with specific frequency bands. Existing and futuristic IoT devices may need many antennas with variable dimensions which might increase the footprint of the device [9]. UWB technology can replace all single narrowband antennas with a unique design [10]. UWB spectrum covers a frequency range from 3.1 GHz to 10.6 GHz and is accepted by the Federal Communications Commission (FCC) [43]. UWB has unique features such as high data rates, straightforward design, low processing power, and operability in short-range communications [44]. Many reports exist on UWB antennas on flexible substrates [9, 45-54]. In this article, new antenna design is investigated for UWB applications. The model is simulated and verified experimentally.

The proposed antenna is fed by CPW transmission line, which is useful for bandwidth enhancement and impedance matching [30]. The overall dimension of the studied antenna is 33.1 mm x 32.7 mm x 0.254 mm with an electrical size  $0.35 \lambda \times 0.35 \lambda$ . The designed antenna covers 3.2-30 GHz (161% fractional bandwidth), the nearly omnidirectional radiation pattern in the whole UWB band. The antenna features a 4.87 dB average peak gain with less than 3 dB gain variations, and 86.61% of average radiation efficiency.

This chapter is organized as follows. Section 3.2 explains the antenna design approaches including the reasons to choose the CPW feeding, impedance matching, and bandwidth

enhancement strategies. Section 3.3 describes the overview of inkjet printing technology, sintering and post-sintering processes to fabricate the antenna. Section 3.4 discusses the simulation and measurement results of the design. Finally, section 3.5 summarize the chapter.

### 3.2 Structure of the Antenna Design

Fig. 3.1 shows the structure (33.1 mm x 32.7 mm x 0.254 mm) of the designed UWB antenna with detailed geometric parameters. The design of the antenna was started by choosing a compatible substrate for IoT applications.

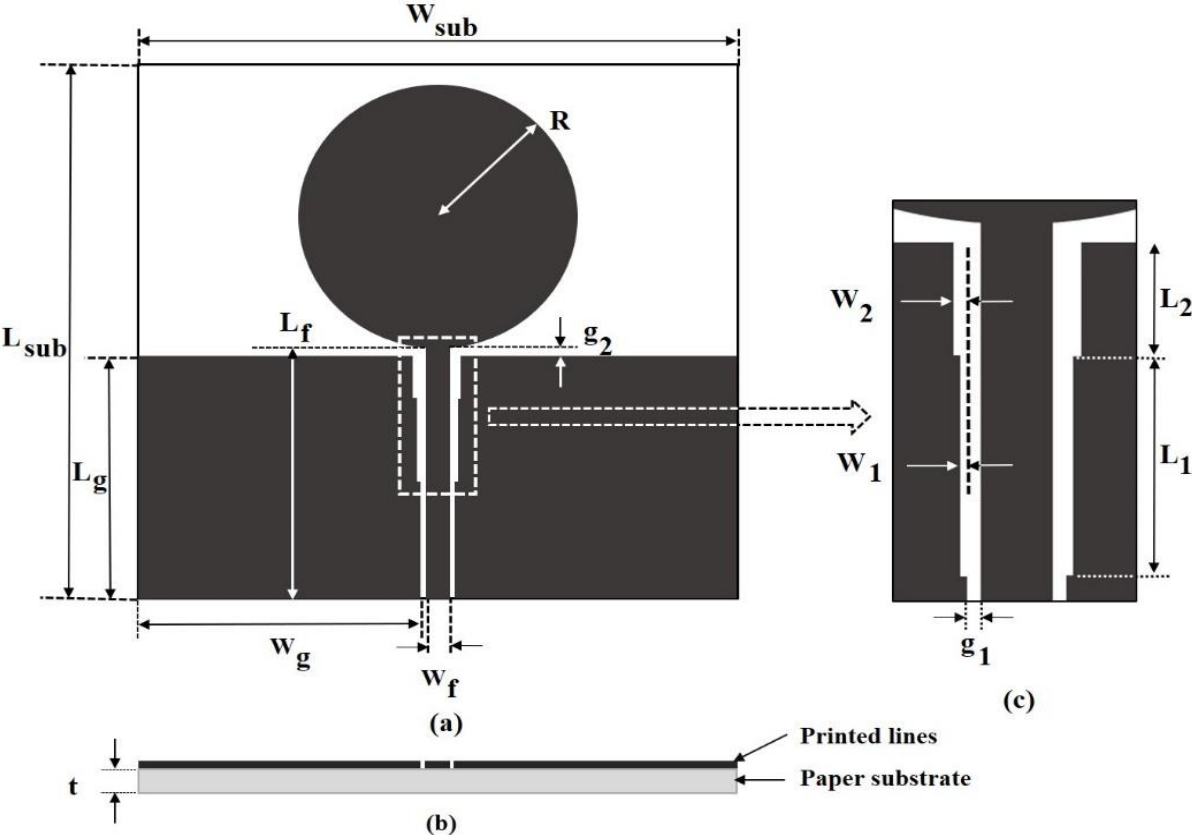


**Figure 3.1.** The geometry of the proposed UWB paper antenna. (a) Top view of the designed antenna, (b) Side view of the antenna looking from the feeding end, and (c) Portions of the down stepped ground plane.

A Kodak photo paper with a thickness of 0.254 mm was selected, which complies robustness, thermal endurance, and flexible operations. The dielectric properties: relative permittivity  $\epsilon_r = 2.85$  and loss tangent  $\tan\delta = 0.05$  was used to design the antenna based on a previous study [55]. As the Kodak paper has a single-side coated printable surface, the CPW feeding technique is ideal where both ground plane and the radiator are printed on the same plane. The CPW feeding significantly cuts down the production cost because of the roll to roll (R2R) fabrication process. Most importantly, it has low radiation loss, improved impedance matching, and broad bandwidth [30]. The antenna pattern utilizes a circular monopole patch for increased bandwidth performance and good radiation characteristics [56].

**Table 3.1** Optimized dimensions of the proposed paper antenna.

Dimension	Value, mm	Dimension	Value, mm
$L_{\text{sub}}$	33.1	$W_{\text{sub}}$	32.7
$L_g$	14.5	$W_g$	16.07
$L_f$	15	$W_f$	1.3
$L_1$	5	$W_1$	0.1
$L_2$	2.6	$W_2$	0.2
$g_2$	0.5	$g_1$	0.2
$R$	7.9	$t$	0.254

The radius of the radiator was calculated using imperial formulas from a circular patch antenna reported in [57] and then optimized in ANSYS HFSS (High-Frequency Structure Simulator). The ground planes formed a down, stepped shape from the feeding end to improve the bandwidth and match the antenna impedance. The dimensions of the CPW line consists of  $g_1$  and  $W_f$  are calculated and optimized later to achieve  $50\Omega$  impedance. Only one geometric parameter of the antenna was tuned at a time while keeping other settings constant. HFSS based simulation achieved the optimum design for a UWB operation. The optimized dimensions of the designed antenna are tabulated in Table 3.1.

### 3.3 Antenna Fabrication

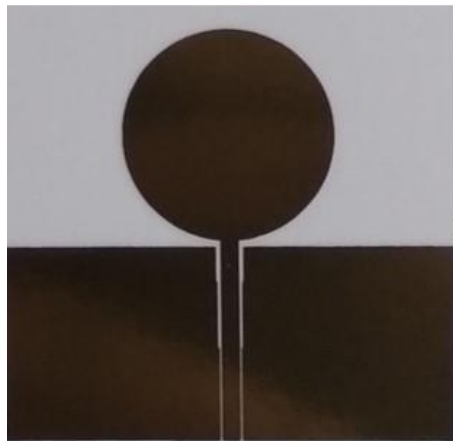
For this research, we utilized the Fujifilm Dimatix 2831 Inkjet printer (DMP), which employs piezoelectric inkjet nozzles, allowing for precision drop-on-demand (DoD) placement. Due to the superior conductivity ( $25 \text{ m}\Omega/\square$ ), long-term stability, firm adhesion, and high-resolution, silver nanoparticles (AgNPs) ink were used for printing, using the 10 pL ink cartridge (DMC-11610) with 1.5 mL of silver nano ink. The optimum printing properties were secured based on an earlier article [58].

After achieving the optimal antenna design employing HFSS, creating a .DXF file, which then converted to the bitmap format using ACE3000 V7 software and uploaded into the DMP program manager. Finally, after setting the printing origin with the fiducial camera printing command can be administered. Later printing, the printed samples were placed over the hot plate to reduce the coffee ring effect and improve the conductivity. The total cure time of the antennas was 30 minutes at  $90^\circ\text{C}$ . The measured conductivity was computed to be  $5.73 \times 10^6 \Omega^{-1}\text{m}^{-1}$ . Fig.

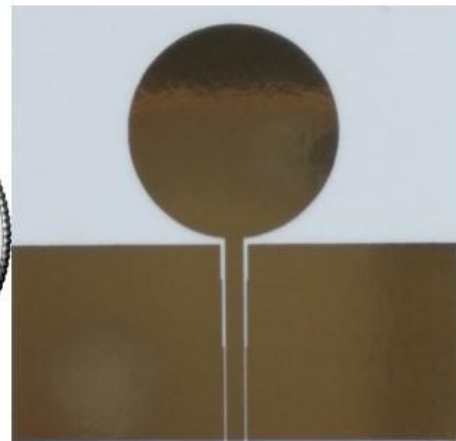
3.2 showcases the photographs of the printed antenna at different stages (antenna fabrication utilizing Dimatix inkjet printer, air curing conditions, and cured conditions).



(a)



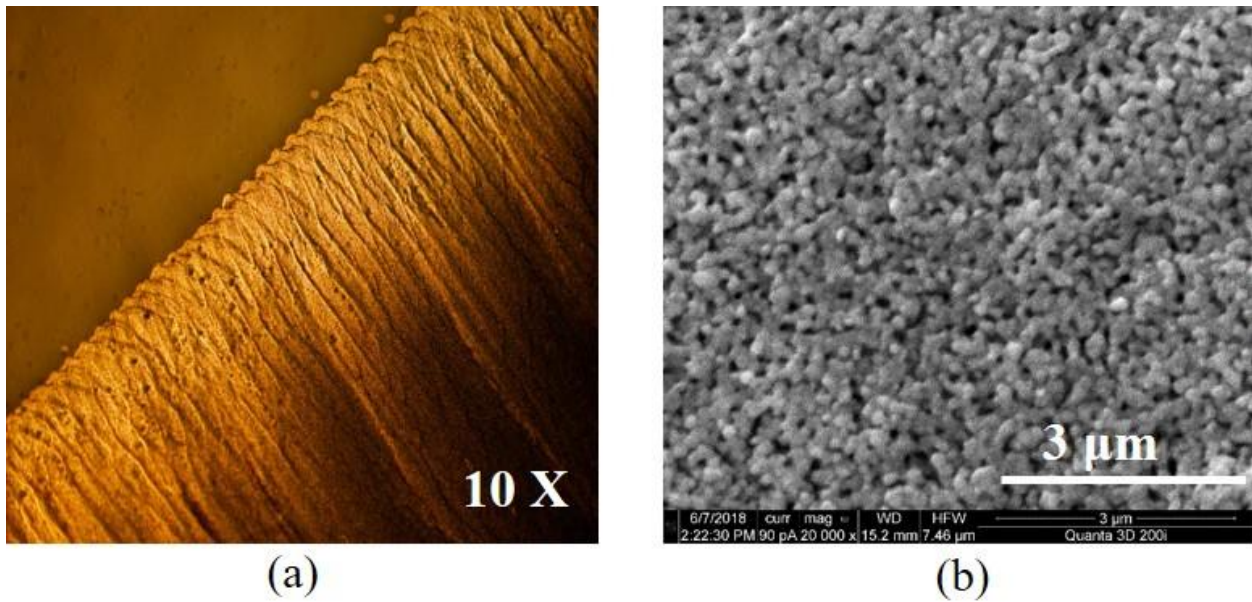
(b)



(c)

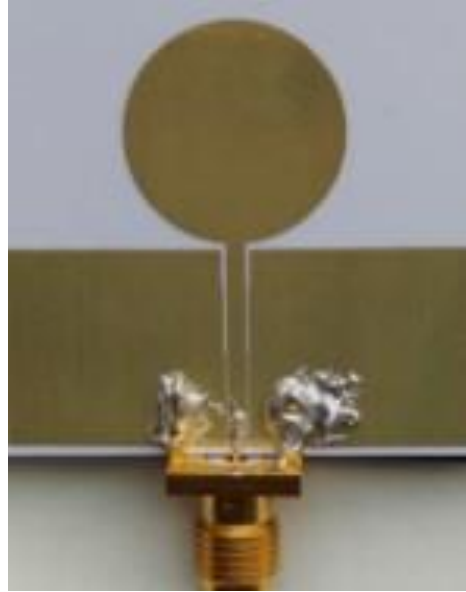
**Figure 3.2.** Inkjet printed antenna on the paper substrate with silver nanoparticles ink. (a) During printing utilizing Fujifilm’s Dimatix 2831 inkjet printer, (b) The prototype of the printed antenna (darkish brown color, before curing), and (c) Fabricated tan colored of the same antenna after curing.

A compound microscope (Nikkon MM 400) was used at 10 X magnification level to inspect the effects of thermal treatment on the surface morphology of the sintered antennas. To further verify the microstructural variations, the scanning electron microscope (SEM), Quanta 3D 200i at 20000X magnification level was used. The CD microscopic image, as revealed in Fig. 3.3(a) indicates the absence of cracks, satellite spots, pinholes, and air bubbles. The SEM image shows uniform ink distribution on paper, as shown in Fig. 3.3(b).



**Figure 3.3.** Surface morphology of the printed pattern after sintering. (a) Compound microscopy (CD) image of the printed pattern and the surface to observe any ink deposition, holes, crack, and coffee ring effect at 10X magnification level, and (b) SEM image of the microstructural variations of the printed silver nanoparticles ink on the paper substrate at 20000X magnification level.

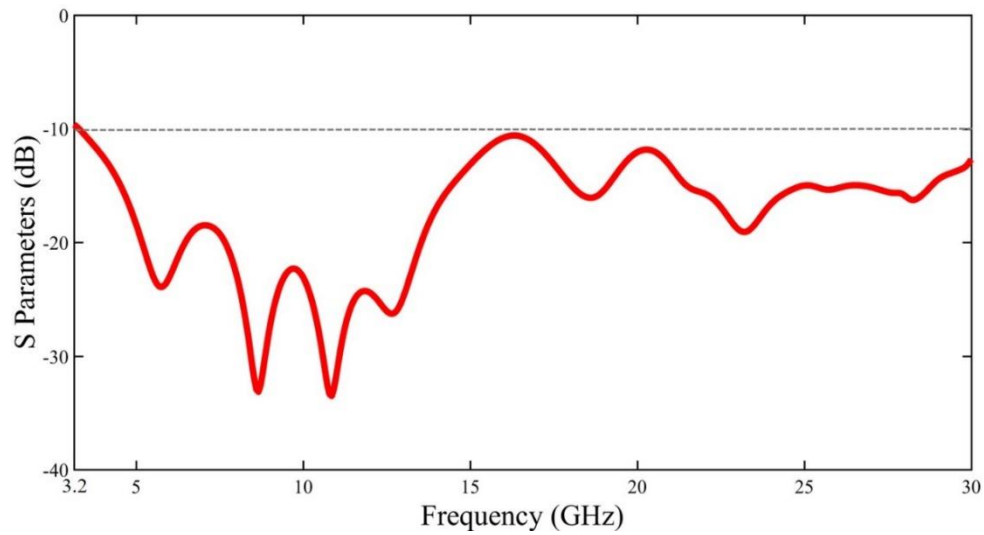
For the feeding signal, the printed antenna was affixed to a sub-miniature version A (SMA) connector using a two-part silver conductive epoxy (8331 14G, MG Chemical) with ratio 1:1 and dried at room temperature. Fig. 3.4 represents the fabricated antenna.



**Figure 3.4.** The CPW-fed fabricated UWB paper antenna.

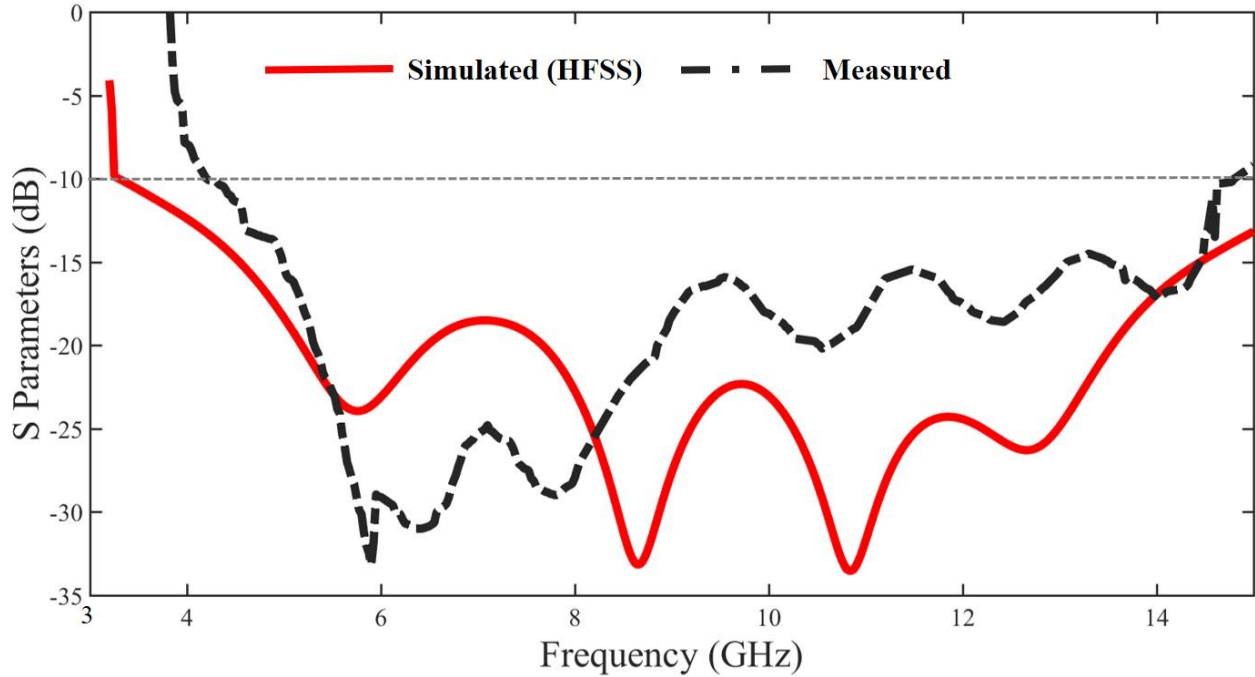
### 3.4 Results and Discussion

The printed antenna was tested with the Agilent PNA-L N5230C vector network analyzer (VNA).



**Figure 3.5.** Simulated reflection coefficient in dB of the proposed antenna as a function of frequency.

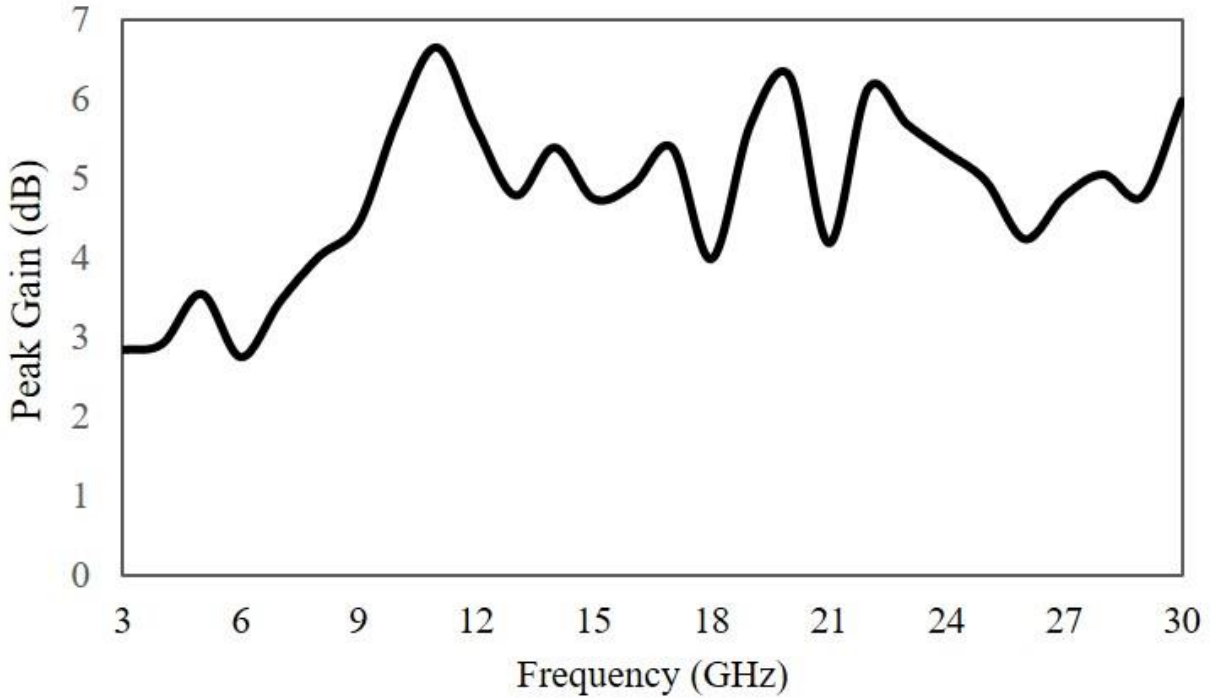
The simulated result of the antenna under test (AUT), as shown in Fig. 3.5, indicates the robust S Parameter ( $S_{11}$ ) with return loss less than -10 dB (Voltage standing wave ratio, VSWR < 2) over a whole impedance bandwidth of 3.2 - 30 GHz. However, the antenna was tested experimentally at 3 - 15 GHz range due to the operational limitations of the VNA.



**Figure 3.6.** Simulated and measured reflection coefficients in dB of the proposed antenna as a function of frequency.

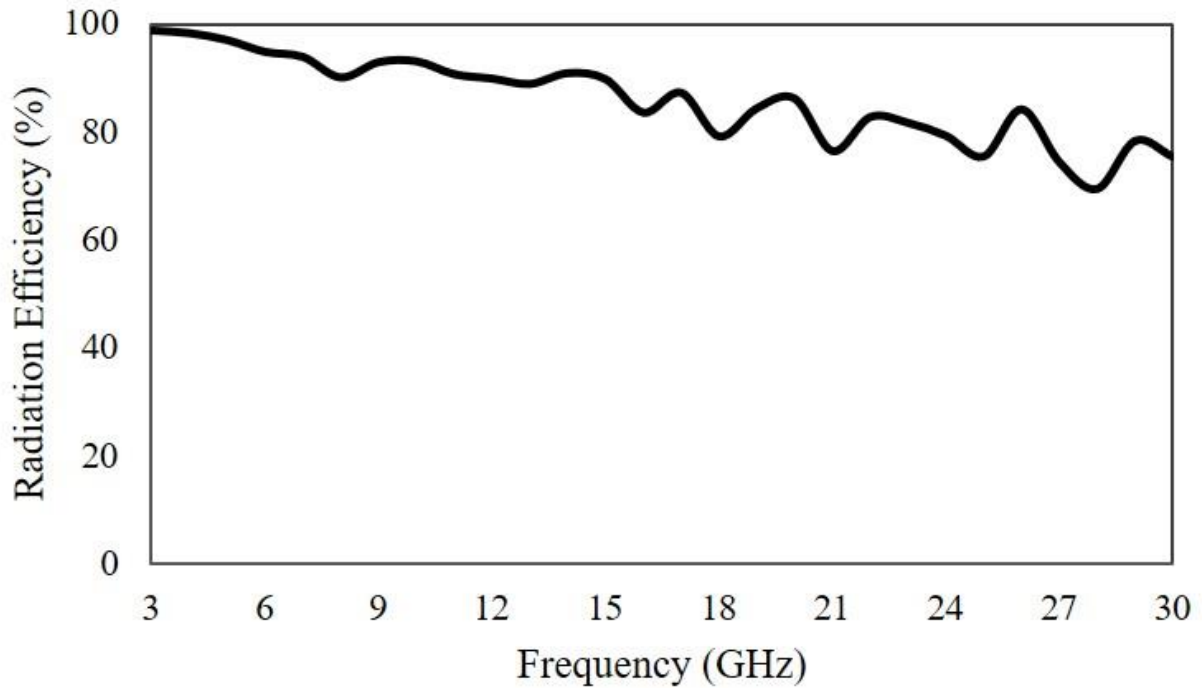
Fig. 3.6 represents the simulated and experimental reflection coefficient of the AUT. The results seem to be in good agreement, with a slight variation in the strength of the resonance and mismatch of return loss values. The discrepancies could be attributed to the uneven size of Ag nanoparticles in ink, AgNp ink deposition, SMA connector losses, the effectiveness of silver epoxy, and measuring environment, and relatively more dielectric loss factor (0.05) of the paper substrate.

Fig. 3.7 indicates the simulated peak gain variations of the antenna as a function of frequency. As observed, the antenna has an average peak gain of 4.87 dB, and gain variations seem to be within 3 dB of the operating frequency range. On the other hand, the radiation efficiency appears



**Figure 3.7.** Simulated peak gain plot as a function of frequency.

to decline with an increase in frequency, as seen in Fig. 3.8. Overall, peak gain versus frequency is an upward trend plot. Whereas, radiation efficiency moves to downward slightly with an increase in frequency, as seen in Fig. 3.7. With an increase in frequency, the geometry of the patch becomes larger than the corresponding wavelength. The observations are consistent with the earlier findings [59, 60]. The average radiation efficiency was found to be of 86.61%.



**Figure 3.8.** Simulated radiation efficiency plot as a function of frequency.

The simulated 2D radiation patterns of the designed CPW antenna in co-polarized and cross-polarized radiated fields are given in Fig. 3.9 at 4.0 GHz frequency in the  $\varphi = 0^\circ$  and  $\varphi = 90^\circ$  planes. The cross-polarization values are 10 to 20 dB lower than the co-polarized values. Figs. 3.10, 3.11, and 3.12 represent similar plots at 6.2, 9.2, and 26.0 GHz frequencies respectively. From these plots, the antenna characterizes a reasonable omnidirectional radiation property for the  $E_\varphi$  components and nearly figure of eight (8) shaped in the  $E_\theta$  components. As expected for the 26.0 GHz, the radiation patterns appear to be distorted and directional. The large physical size of the antenna at higher frequencies with reduced wavelength could explain such distortions, and the outcomes are consistent with the earlier findings [61, 62].

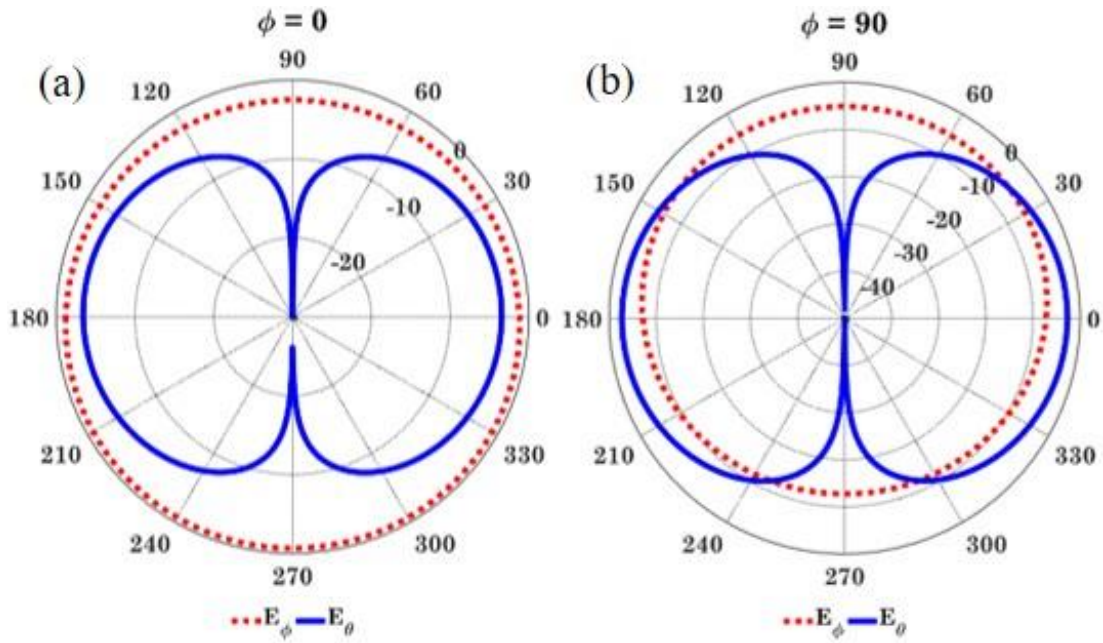


**Figure 3.9.** Simulated radiation pattern of the antenna at 4.0 GHz for a)  $\phi = 0^\circ$  and b)  $\phi = 90^\circ$  planes.

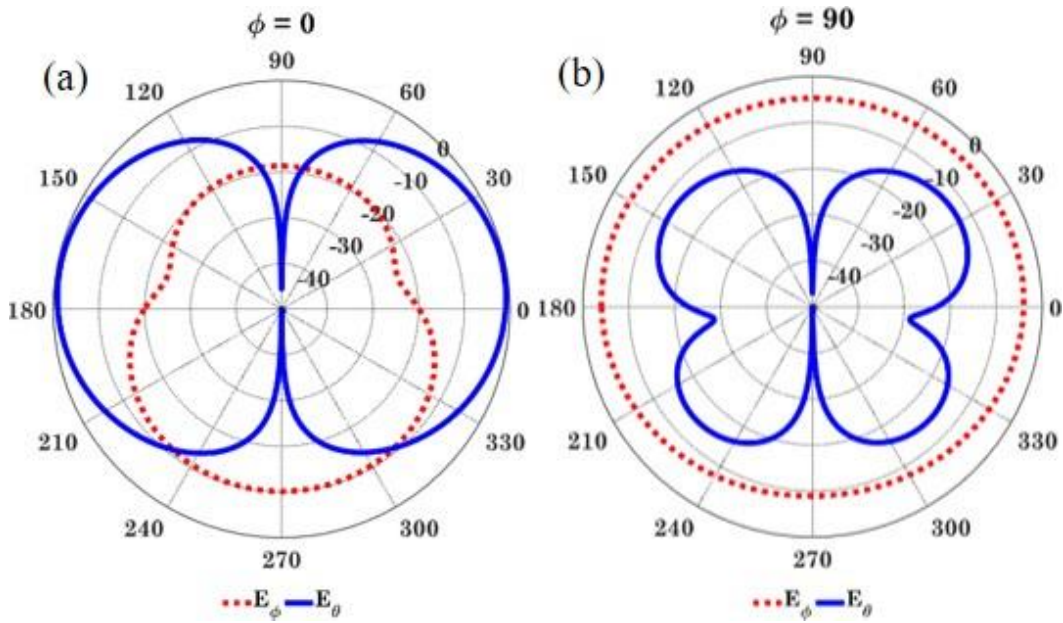


**Figure 3.10.** Simulated radiation pattern of the antenna at 6.2 GHz for a)  $\phi = 0^\circ$  and b)  $\phi = 90^\circ$  planes.

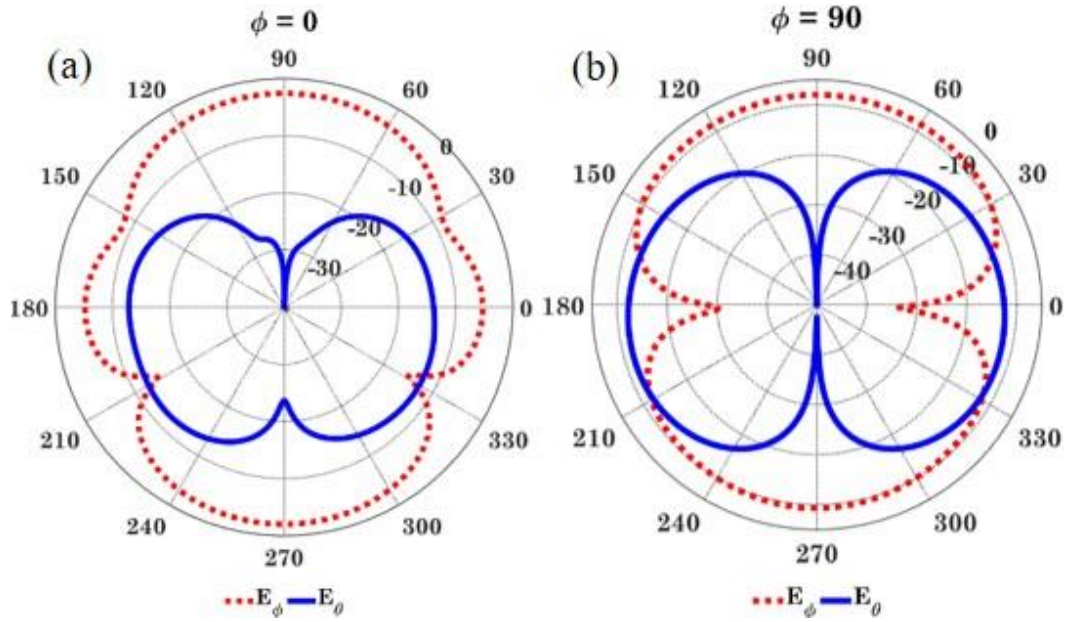


**Figure 3.11.** Simulated radiation pattern of the antenna at 9.2 GHz for a)  $\phi = 0^\circ$  and b)  $\phi = 90^\circ$  planes.

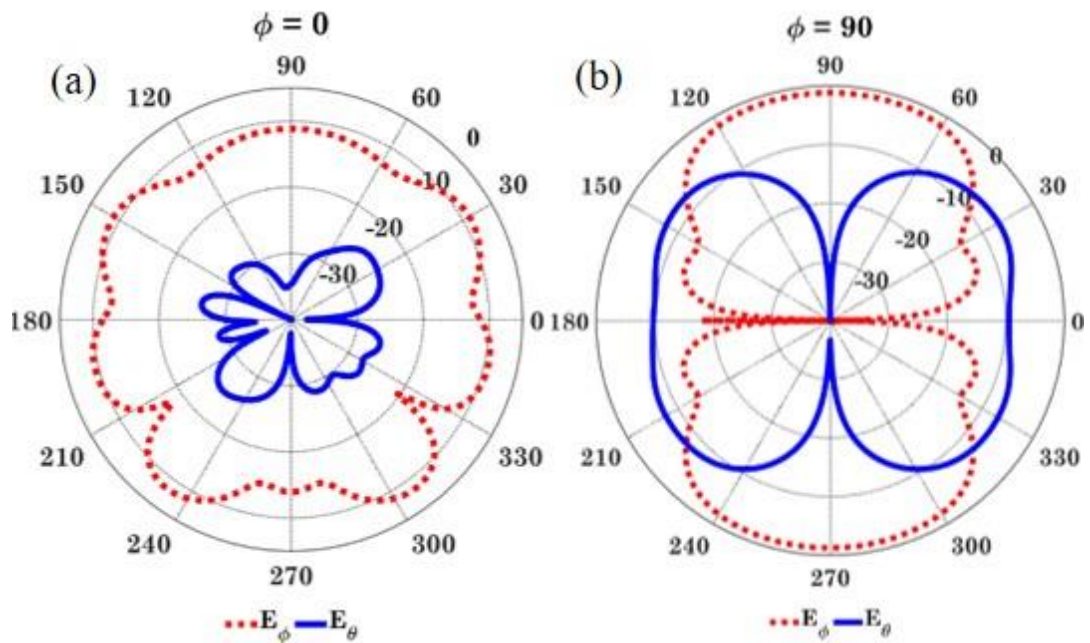
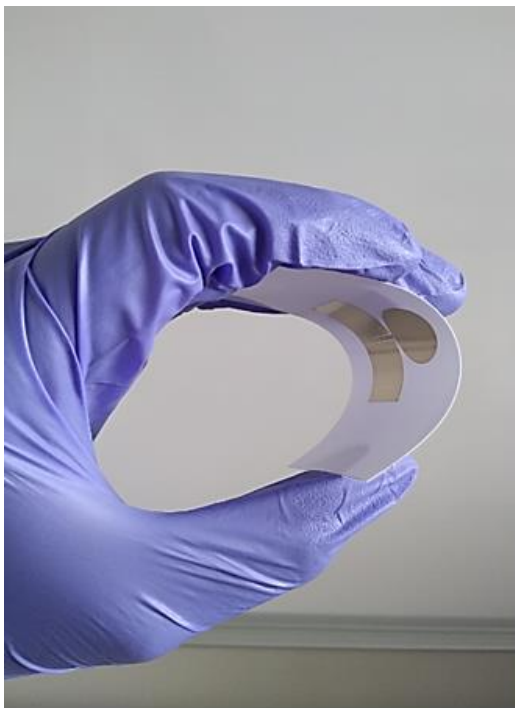


**Figure 3.12.** Simulated radiation pattern of the antenna at 26.0 GHz for a)  $\phi = 0^\circ$  and b)  $\phi = 90^\circ$  planes.

The investigated antenna was intended for IoT and wearable applications, and hence the AUT must pass the rolling and bend test. Bending of the substrate seems to affect the electrical conductivity. We experimented printed samples at five discrete bending conditions. Two different forms of bending test out of five are depicted in Fig. 3.13. The resistivity variations in-situ (using two-point probe method) and after repeated bending test (using the four-point probe method) were limited to  $\pm 0.5\%$ . The antenna was bent horizontally and vertically, and with a tiny variation on resistivity ( $\pm 0.5\%$ ) the scattering parameters are expected to be within range. Flexibility along with minimal resistivity fluctuations suggests that the investigated antenna will be conducive for wearable and IoT applications.



(a)



(b)

**Figure 3.13.** Bending test (a) deformed using human hand and (b) roll bending

### **3.5 Summary**

In this chapter, a flexible 254  $\mu\text{m}$  thick UWB antenna is fabricated on a paper substrate is presented. The designed antenna derives from a CPW feedline by loading a circular radiator and down stepping the ground plane to enhance the bandwidth. The proposed monopole antenna is of dimensions 33.1 mm x 32.7 mm x 0.254 mm. Based on the optimized antenna architecture, a prototype of the proposed antenna was fabricated and validated experimentally. Both the simulated and experimental results are in good agreement. The antenna exhibits nearly omnidirectional radiation patterns with slight gain variations in the whole UWB band. The antenna's compliance with UWB requirements and flexible characteristics of the paper substrate makes it a suitable candidate for the commercial wearable and IoT applications.

## CHAPTER 4: A COMPACT MONOPOLE ANTENNA FOR ULTRA-WIDEBAND (UWB) APPLICATIONS

### 4.1 Background

With an increase in the use of multipurpose wireless communication systems, ultra-wideband (UWB) antennas are becoming popular in future communication systems since its adaptation by Federal Communications Commission (FCC) in 2002 [43]. According to the FCC, the UWB antenna exceeds the minimum bandwidth of 500 MHz or 20% of the center frequency. UWB systems offer other advantages such as high data rates with low manufacturing cost, simple design features, low power consumption, and operability in short and long-range frequency spectrum. Further, the UWB antenna can be used to replace multiple narrowband single antennas [63]. At present, microstrip patch antenna design is popular in communication devices due to its easy integration with Monolithic Microwave Integrated Circuits [64].

In recent years, various UWB antennas have been investigated with microstrip patch antenna design [65-72]. But, few have accounted for the wide impedance bandwidth while maintaining higher radiation efficiency. In addition, the electrical and physical dimensions of the investigated UWB antenna are largely preventing its use in compact applications. An antenna with coplanar waveguide (CPW)-fed and a pair of symmetry curved radiating slot was analyzed for UWB applications to cover a bandwidth of 3-20 GHz with electrical dimensions of  $0.64\lambda \times 0.4\lambda$  [73]. In another report [74], a CPW-fed UWB antenna was presented, which covers a bandwidth of 3-30 GHz and electrical dimension of  $0.39\lambda \times 0.47\lambda$ . Singhal et al. [59] investigated a hexagonal fractal antenna with 3.4-37.4 GHz bandwidth and electrical dimension of  $0.32\lambda \times 0.34\lambda$ . A fractal microstrip antenna was reported by Azari [75], which operates from 10 GHz to 50 GHz with

electrical aspects of  $2\lambda \times 2\lambda$ . An elliptical monopole antenna with trapezoid ground plane and bandwidth 1.02-24.1 GHz has been reported by Liu et.al [76]. It has large electrical dimensions and low gain at low frequencies. Further, a microstrip patch antenna has been studied and designed for multiple purposes in wireless communications [77]. This antenna operates in the bandwidth from 4.0 GHz to 19.8 GHz. The results of this study were based on just simulation. The investigated antennas though cover a relatively large frequency spectrum, however, occupy large electrical dimensions.

In this chapter, a compact UWB antenna is designed, simulated, fabricated, and tested. The antenna design was inspired by a previous study [77]. Significant improvements on this design are made by optimizing the antenna parameters, inserting slot in the feedline, and impedance matching. The designed antenna covers 4-40 GHz (164% fractional bandwidth), exhibits nearly omnidirectional radiation patterns over the entire impedance bandwidth with more than 2.8 dB peak gain and 75% of average radiation efficiency. The investigated antenna is electrically and physically compact, easy to design and fabricate in comparison to previously reported antennas. The investigated antenna design overcomes the limitations of UWB antennas such as narrow impedance bandwidth, large electrical dimension, and low gain reported earlier.

## **4.2 Structure of the antenna design**

The geometric structure of the proposed UWB monopole antenna is shown in Figure 4.1. The designed antenna is printed on a 1.4 mm thick FR-4 epoxy substrate with relative permittivity  $\epsilon_r = 4.4$  and loss tangent  $\tan\delta = 0.02$ . The physical dimension of the antenna is 28.1 mm x 17.1 mm x 1.4 mm. The conductive radiating patch is printed on the top side of the FR-4 substrate, whereas the finite slotted ground plane is printed on the other side of the same substrate.

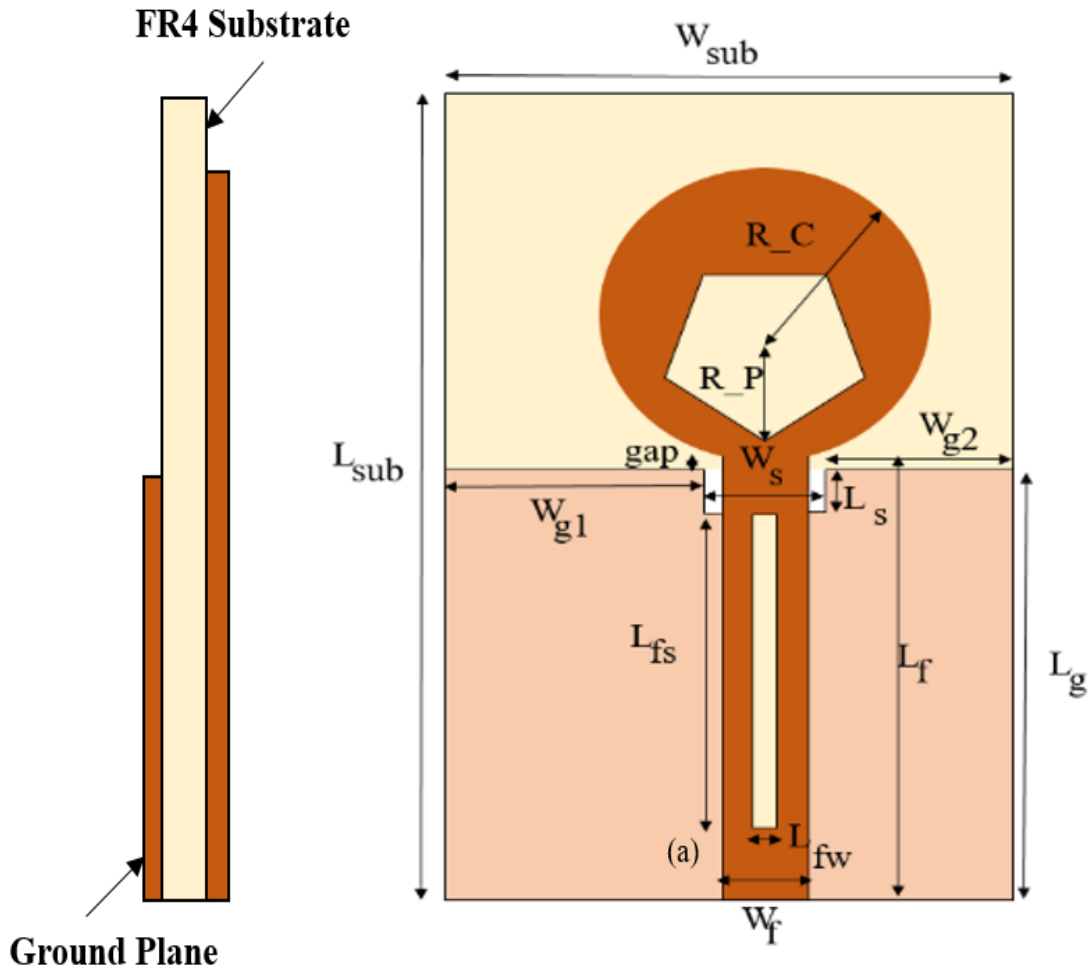


**Figure 4.1.** Geometry of the designed antenna

The antenna pattern utilizes the circular patch for increased bandwidth performance; whereas the radius of the patch is related to the operating frequency and the input impedance of the antenna. The radius of the patch was calculated applying imperial formulas of circular patch antenna given in [57] and then optimized using ANSYS HFSS (High-Frequency Structure Simulator) software. To further improve the bandwidth (besides adopting the finite ground plane and circular radiator), a pentagon-shaped slot is embedded into the radiating patch without compromising the overall dimensions of the antenna. The dimensions of the rectangular microstrip

feed line is calculated initially based on a previous design [78] and then optimized. The feed line is shifted right slightly from the center of the substrate, and a rectangular slot is cut into it to improve impedance matching.

**Table 4.1.** Optimized dimensions of the designed UWB antenna

Dimension	Value, mm	Dimension	Value, mm
$L_{\text{sub}}$	28.1	$W_{\text{sub}}$	17.1
$L_{\text{g}}$	15.04	$W_{\text{g1}}$	8
gap	0.2	$W_{\text{g2}}$	5.6
$L_{\text{s}}$	1.5	$W_{\text{sub}}$	3.5
$L_{\text{f}}$	15.26	$W_{\text{f}}$	2.62
$L_{\text{fs}}$	14.5	$L_{\text{fw}}$	0.7
$R_{\text{C}}$	5.04	$R_{\text{P}}$	3.2

To match the impedance and enhance the impedance bandwidth further, a notch is etched out from the ground plane [79]. Only one dimension of the antenna was adjusted at a time while keeping other parameters constant. The optimum design for a wide frequency range operation was obtained by HFSS based simulation. The optimized values of the various dimensions of the investigated planar monopole antenna are given in Table 4.1.

### 4.3 Results and discussion

The antenna is designed and simulated using finite element method (FEM) based ANSYS HFSS. The optimized antenna is fabricated with an LPKF S63 milling machine in the Radio Frequency (RF) Research Laboratory at Washington State University Vancouver to verify the simulated results. The antenna prototype, as seen in Figure 4.2, was tested with the Agilent PNA-L N5230C network analyzer.

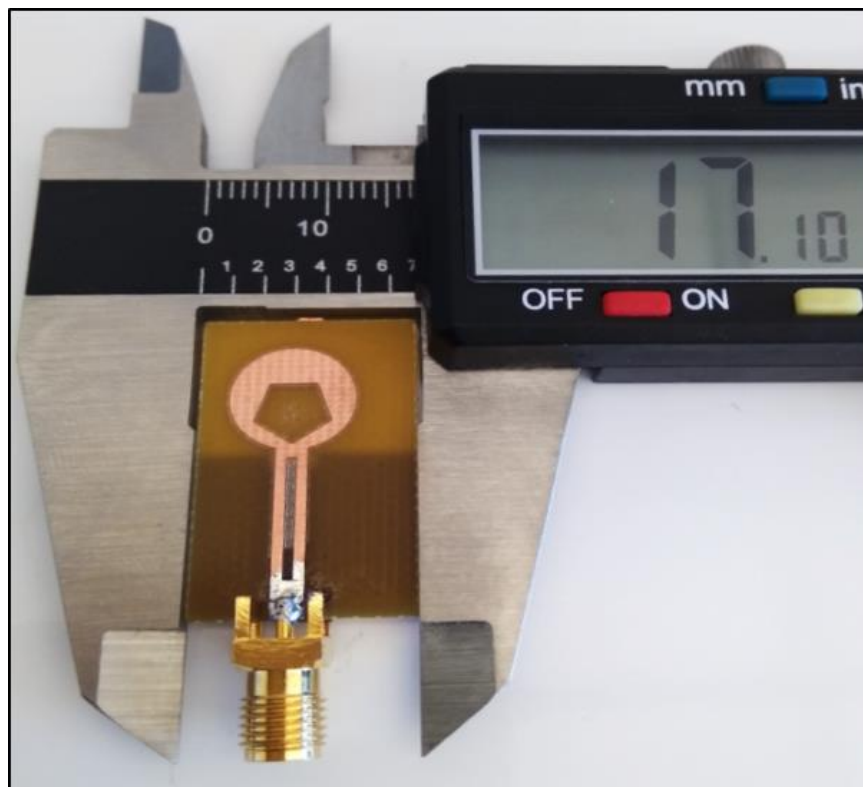


**Figure 4.2.** The fabricated UWB antenna

The simulated results (Figure 4.3) of the antenna indicates strong S Parameter ( $S_{11}$ ) with return loss less than 10 dB (Voltage standing wave ratio,  $VSWR < 2$ ) over a wide bandwidth 4 - 40 GHz. However, the antenna was tested experimentally from 4 - 20 GHz range due to the operational limitations of the network analyzer.

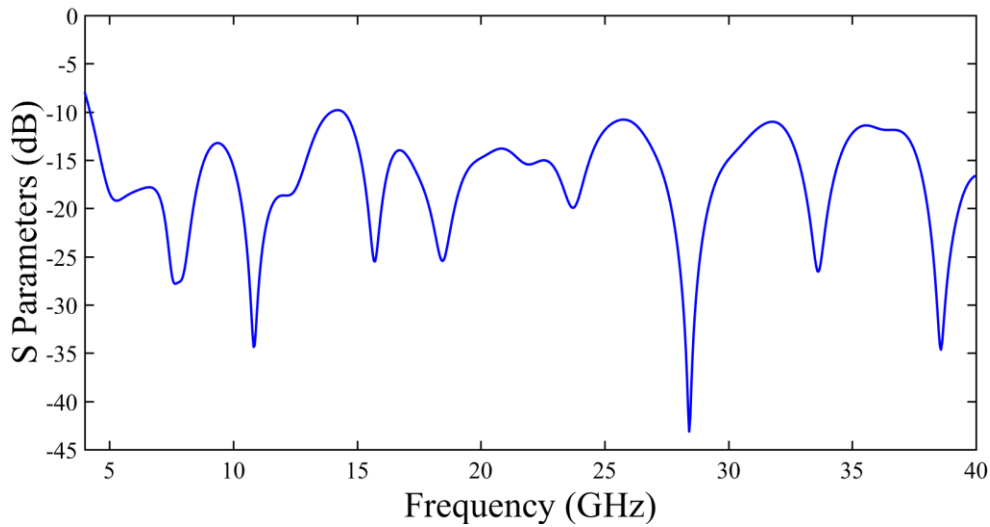


**Figure 4.3.** Simulated return loss of the designed antenna

As seen from Figure 4.4, the simulated and experimental results are in good agreement for the 10 dB return loss (up to 20 GHz). It can be inferred from the figure that most of the resonant frequencies of simulated and measured results matched. However, the return loss graph of experimental results shifted upward (as compared to simulation).

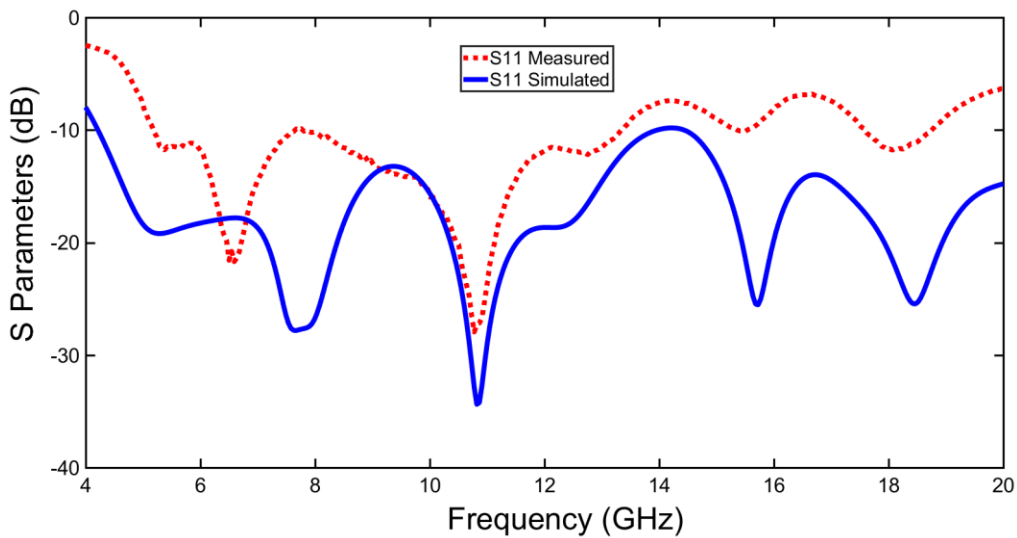


**Figure 4.4** Simulated and measured return loss of the designed antenna

Such a discrepancy can be attributed to manufacturing tolerances, SMA connector losses, measuring environment, and FR-4 substrate losses, particularly at the higher frequencies. Similar phenomena can be noticed for the VSWR plot, as depicted in Figure 4.5.

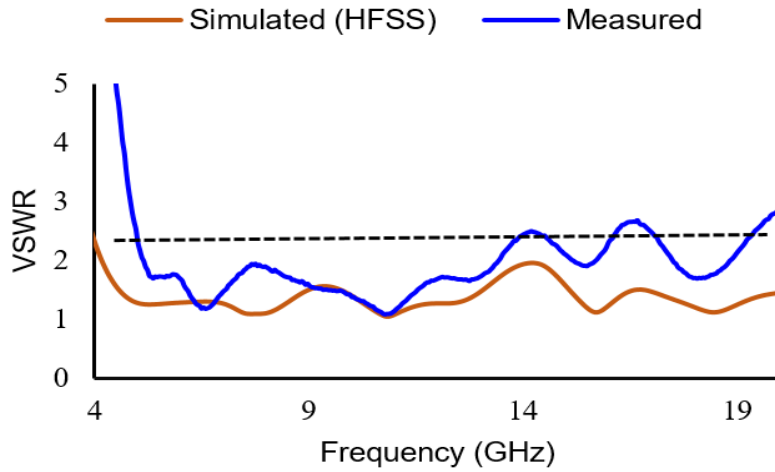


**Figure 4.5** Simulated and measured VSWR of the designed antenna

The simulated peak gain of the antenna as a function of frequency is shown in Figure 4.6. As observed, the antenna has a peak gain of 2.8 dB and above for the entire frequency band

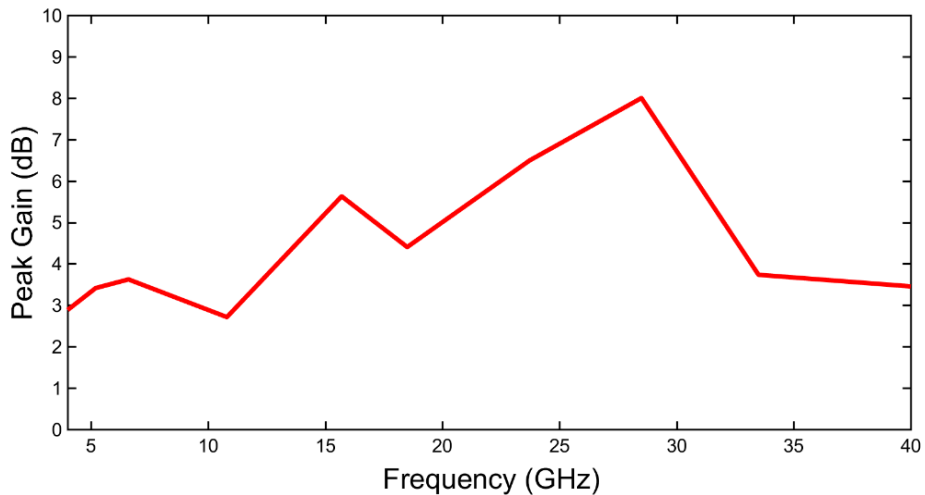


**Figure 4.6** Simulated peak gain plot as a function of frequency

With an increase in frequency, the peak gain seems to increase until 28.5 GHz. The maximum peak gain is observed to be 8 dB at 28.5 GHz.

From the frequency versus radiation efficiency plot (Figure 4.7), it appears that the radiation efficiency seems to decrease with an increase in frequency [61]. The average radiation efficiency was found to be of 75%. Observations from Figure 4.6 and 4.7 are consistent with an earlier finding that the geometry of the structure becomes larger than the corresponding wavelength [59].

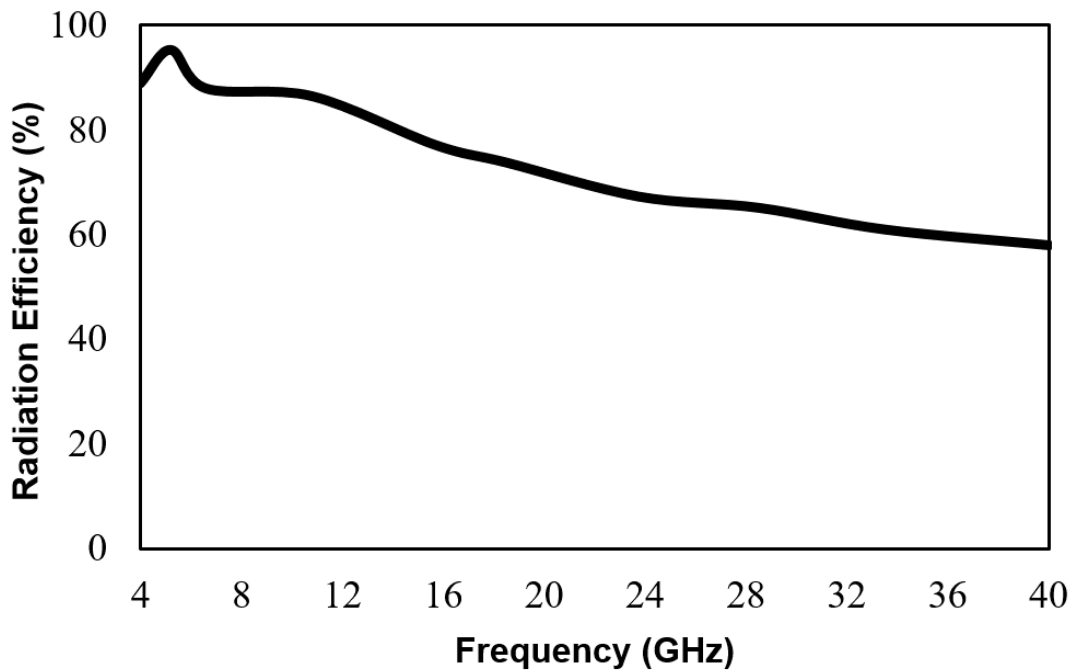


**Figure 4.7.** Simulated radiation efficiency plot as a function of frequency

The simulated 2D radiation patterns of the designed monopole antenna in co-polarized and cross-polarized radiated fields are shown in Figure 4.8 (a) and 4.8 (b) at 5.2 GHz frequency in the  $\phi = 0^\circ$  and  $\phi = 90^\circ$  planes. The cross-polarization values are 15 to 30 dB lower than the co-polarized values respectively. Similar radiation characteristics are found for the 10.8 GHz, as seen in Fig.

4.9 (a) and 4.9 (b). For the 28.5 GHz frequency plot, the radiation patterns appear to be distorted and directional, as presented in Fig. 4.10 (a) and 4.10 (b). The large physical size of the antenna at higher frequencies with reduced wavelength could explain such distortions [61, 62].

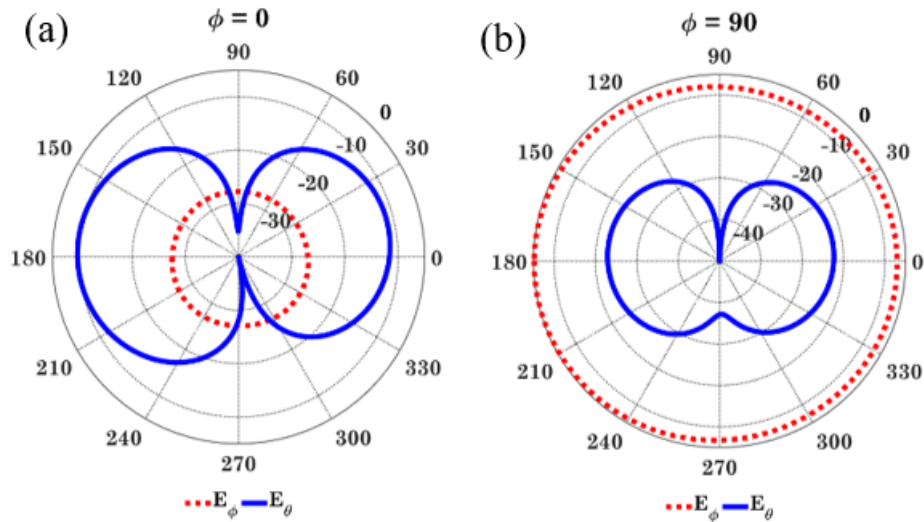


**Figure 4.8.** Radiation pattern of the antenna at 5.2 GHz for a)  $\phi = 0^\circ$  and b)  $\phi = 90^\circ$  planes

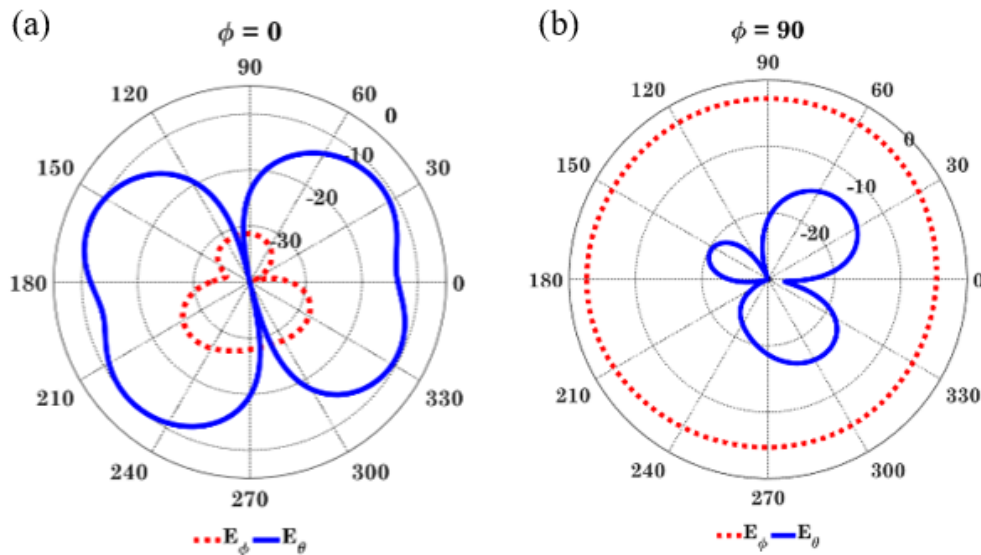


**Figure 4.9.** Radiation pattern of the antenna at 10.8 GHz for a)  $\phi = 0^\circ$  and b)  $\phi = 90^\circ$  planes

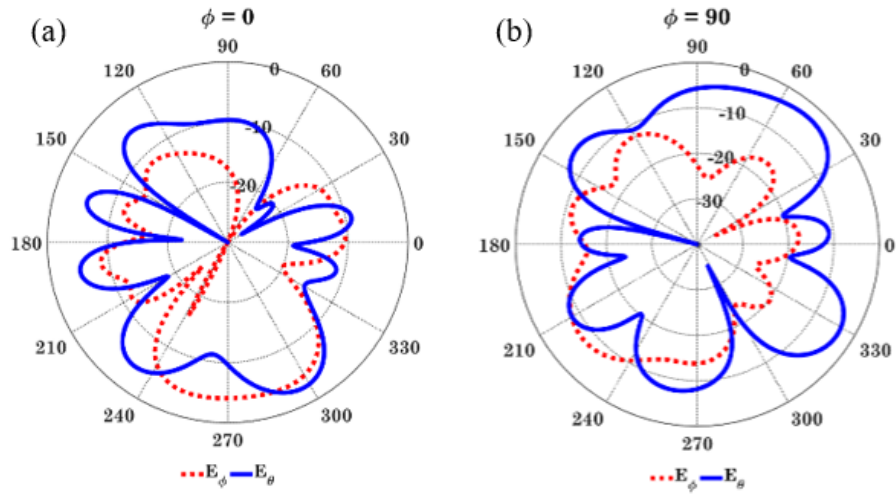


**Figure 4.10.** Radiation pattern of the antenna at 28.5 GHz for a)  $\phi = 0^\circ$  and b)  $\phi = 90^\circ$  planes

The 3D radiation pattern of this designed antenna at various frequencies are shown in Figure 11.

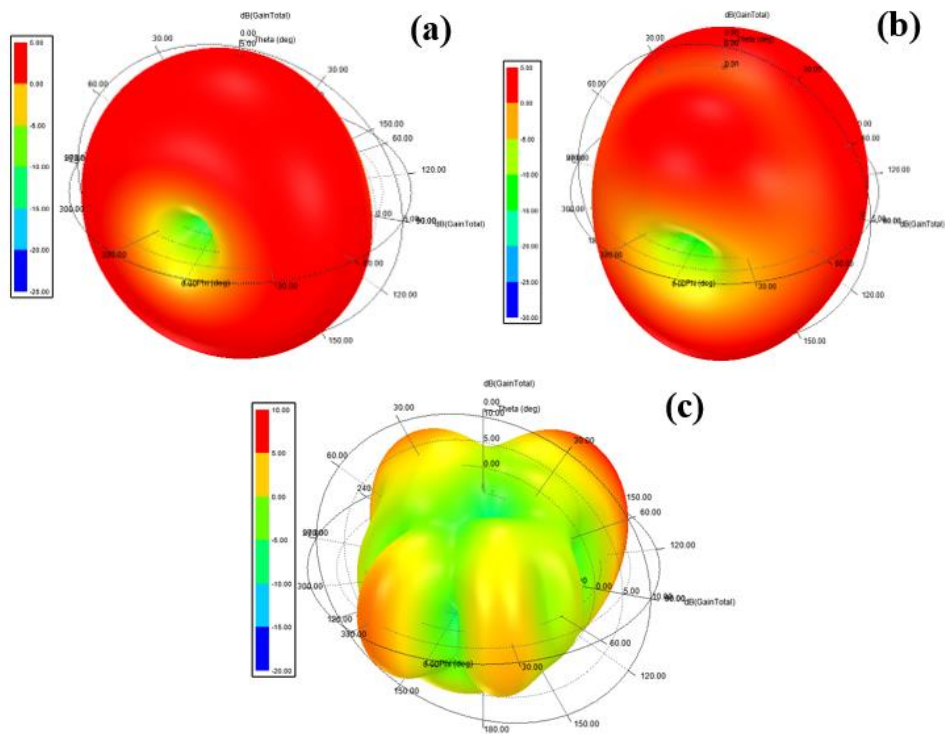


**Figure 4.11.** 3D Simulated radiation pattern of the designed antenna at (a) 5.2 GHz, (b) 10.8 GHz, and (c) 28.5 GHz frequency.

#### 4.4 Summary

A printed planar circular monopole antenna is presented in this chapter for UWB applications. The designed antenna is derived from a microstrip feedline by loading the slotted circular radiator and slotted finite ground plane to establish the wideband. Based on the optimized antenna geometry, the antenna was fabricated and tested. The resonant frequencies of the experimental and simulated results appear to match. The UWB antenna covers over 4-40 GHz (164% fractional bandwidth) range with a return loss of 10 dB or more (VSWR <2). The antenna exhibits a relative omnidirectional radiation pattern with more than 2.8 dB peak gain for the entire frequency spectrum and average radiation efficiency of 75%. The simulated antenna performance and experimental results indicate the suitability of this antenna in UWB communications along with C, X, K<sub>u</sub>, K, K<sub>a</sub>-band, WLAN and future wireless services.

# CHAPTER 5: BEAM-STEERABLE MODIFIED BOW-TIE ANTENNA ARRAY FOR 5G COMMUNICATIONS

## 5.1 Background

Due to the limitations of the existing shorter frequency bands (< 10 GHz) regarding high traffic and communication network speed, the next generation (5G) wireless communication wave is required to secure highly reliable ubiquitous connectivity with massive volumes and diversity of data. Compared with the previous generations, 5G cellular communications will use higher frequency bands ranging from 10 GHz to 80 GHz with broader communication bandwidth [11]. However, with the increase of operating frequencies would bring new challenges to design and implement the antennas into the future handheld devices [12]. Taking into account all the designing and implementing challenges, many countries across the globe have been starting to assign their distinct frequency spectrum to carry out their research and speed up the 5G development [80].

In recent years, many 5G antennas have been studied and investigated with microstrip antennas including phased array systems [81-85]. The reason to utilize the phased array antenna is the functionality of point-to-point (PtP) communication between the base station and the remote handheld devices [82]. On the other hand, microstrip antennas are widely used to design the phased array systems because of their compactness, higher efficiency, and relatively easy integration with Monolithic Microwave Integrated Circuits [57, 60]. Although, the mentioned design offers excellent performance: scanning property and antenna gain over the entire operating range, however, most of the article is based on the simulation and operates in the bandwidth less than 2 [81, 83].

After considering all limitations, this research proposes a new design of microstrip-fed phased array antenna for the future 5G cellular communications. The antenna element chosen in this study is a modified bow-tied design, with each individual antenna consisting of a pair of radiators printed on both sides of the substrates. It is designed and simulated using finite element method (FEM) based ANSYS HFSS (High-Frequency Structure Simulator) software, which covers 16.5-19.5 GHz (16% FBW) frequency range, where input impedance, reflection coefficient, radiation pattern, beam steering characteristics of the antenna were investigated. The peak gain and average radiation efficiency of a single design are 4 dB and 90%. After utilizing the phased array systems, antenna gain improved significantly: 5.2 dBi, 6.2 dBi, and 8 dBi for 1x2, 1x4, and 1x8 array design respectively irrespective to different scanning angles. The separation between the adjacent antenna elements, a crucial parameter, was investigated and set at around  $\lambda/2$  distance to have an excellent mutual coupling, scanning property, and high gain. The investigated antenna is electrically and physically compact, easy to design and fabricate: compatible for the required beam coverage in 5G communications.

This chapter is organized as follows. Section 5.2 explains the configuration and performance of the single element bow-tie antenna. Section 5.3 investigates the distance between adjacent antenna elements and exhibits the simulation results of the final array design with different scanning angles. Finally, section 5.4 summarize the chapter.

## **5.2 Single element modified bow-tie antenna**

The circuit layout of the proposed modified bow-tie antenna is depicted in Fig. 5.1 with detailed geometric parameters. It is a compact and symmetrical structure, which consists of two radiators: one is printed on the top side of the substrate, whereas the other one is printed with the

ground plane on the opposite side of the same substrate. Although ideally, a bow-tie antenna is a triangular structure, however, we add a circular arc with one arm of the triangle to improve the bandwidth of the proposed design. With regards to the opening angle, the other two sides of the triangle can be chosen in the range of  $10\text{-}80^\circ$  [9]. For this design, we tuned this angle in HFSS at  $71^\circ$ , which gives modest frequency response and impedance match.

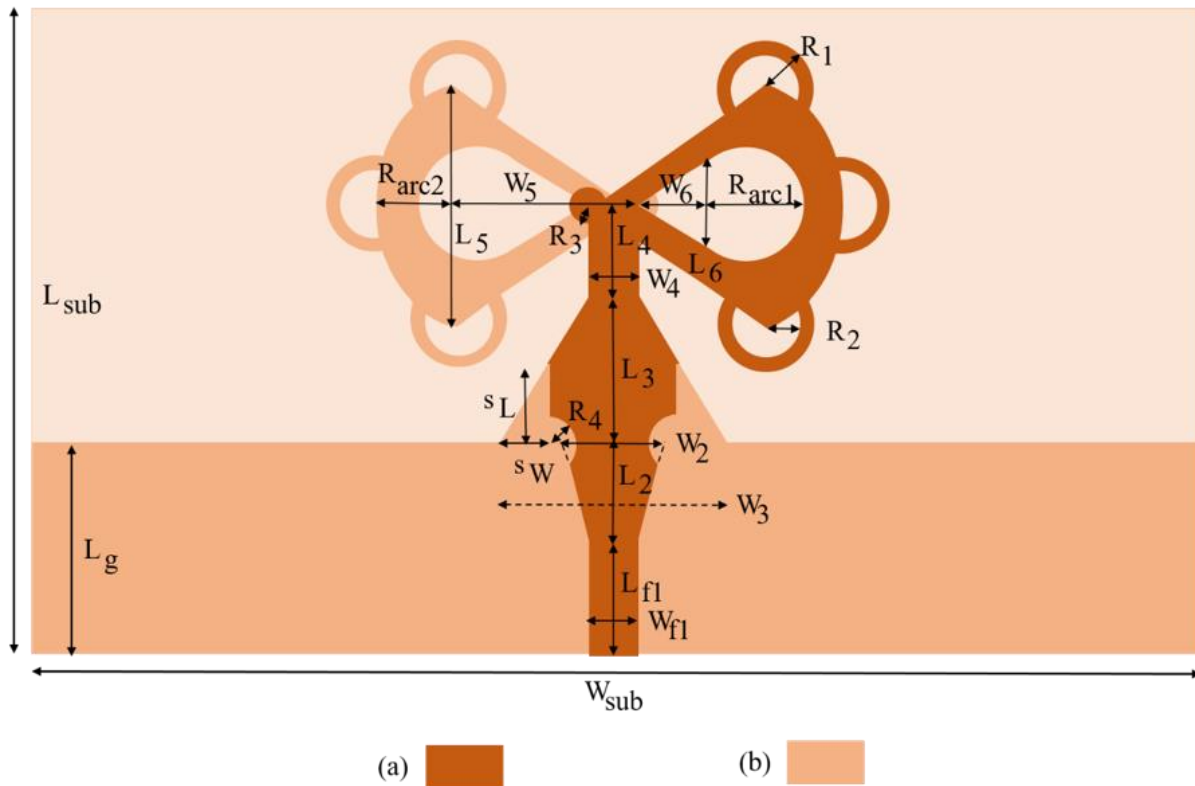


**Figure 5.1.** Proposed 5G modified bow-tie antenna architecture, (a) top layer and (b) bottom layer

As presented in Fig. 5.1, each radiator comprises a total of four opening holes to increase the length of the current path and reduce the overall antenna size. Some little design variations between the two radiating elements are visible; two triangular and two circular slots etched out from the top radiator to match the impedance and improve the bandwidth further. The designed

antenna is printed on a conventional FR-4 epoxy substrate with relative permittivity  $\epsilon_r = 4.4$ , loss tangent  $\tan\delta=0.02$ , and a thickness of 1.5 mm.

**Table 5.1.** Optimized dimensions of proposed 5G antenna

Dimension	Value, mm	Dimension	Value, mm
$L_{sub}$	5.5	$W_{sub}$	10
$L_g$	1.8	$H_{sub}$	1.5
$L_{f1}$	1	$W_{f1}$	0.4
$L_2$	0.8	$W_2$	0.8
$L_3$	1.25	$W_3$	1.9
$L_4$	0.8	$W_4$	0.4
$L_5$	2	$W_5$	1.4
$L_6$	0.86	$W_6$	0.6
$s_L$	0.65	$s_w$	0.45
$R_{arc1}$	0.65	$R_{arc2}$	0.65
$R_1$	0.4	$R_2$	0.25
$R_3$	0.15	$R_4$	0.2

The physical dimension of the antenna is 10 mm x 5.5 mm x 1.5 mm. Only one parameter of the antenna was adjusted at a time while keeping other variables constant. The optimum design for the 5G operation was obtained by HFSS based simulation. The optimized dimensions of the investigated antenna are tabulated in Table 5.1.

The simulated result of the antenna, as seen in Fig. 5.2 indicates robust S Parameter ( $S_{11}$ ) with return loss less than -10 dB and over a full impedance bandwidth 16.65-19.65 GHz (3 GHz) with more than 16% FBW, and Fig. 5.3 depicts a voltage standing wave ratio (VSWR) $<2$ .

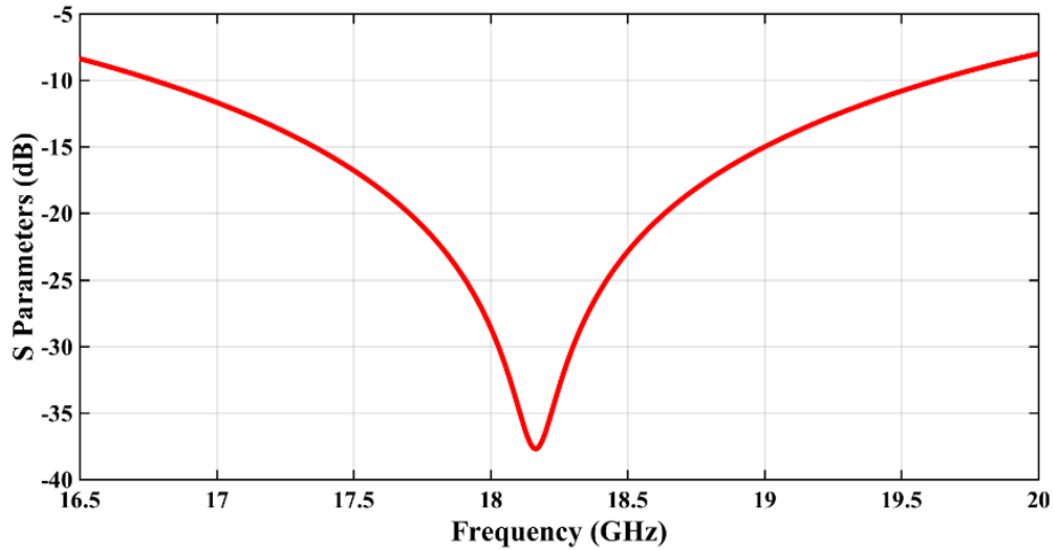


**Figure 5.2.** Simulated return loss results of the 5G modified bow-tie antenna as a function of frequency

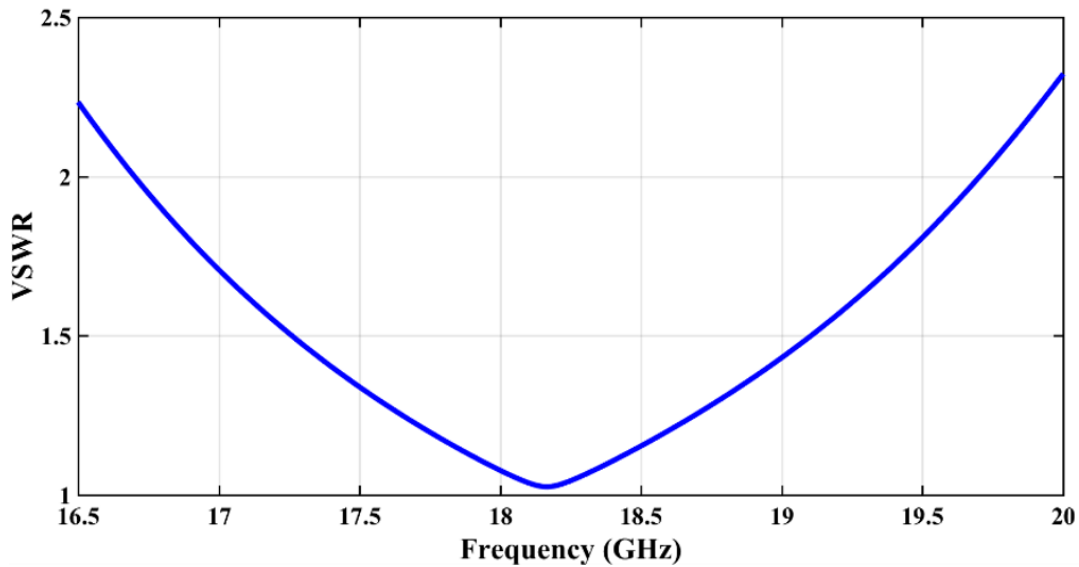


**Figure 5.3.** Simulated return loss results of the 5G modified bow-tie antenna as a function of frequency

Fig. 5.4 and 5.5 showcases the simulated H-field and E-field distribution of the proposed antenna at 18.35 GHz frequency, which shows that most of the current concentrated around the edge regions, and tapered ends of the antenna arms.

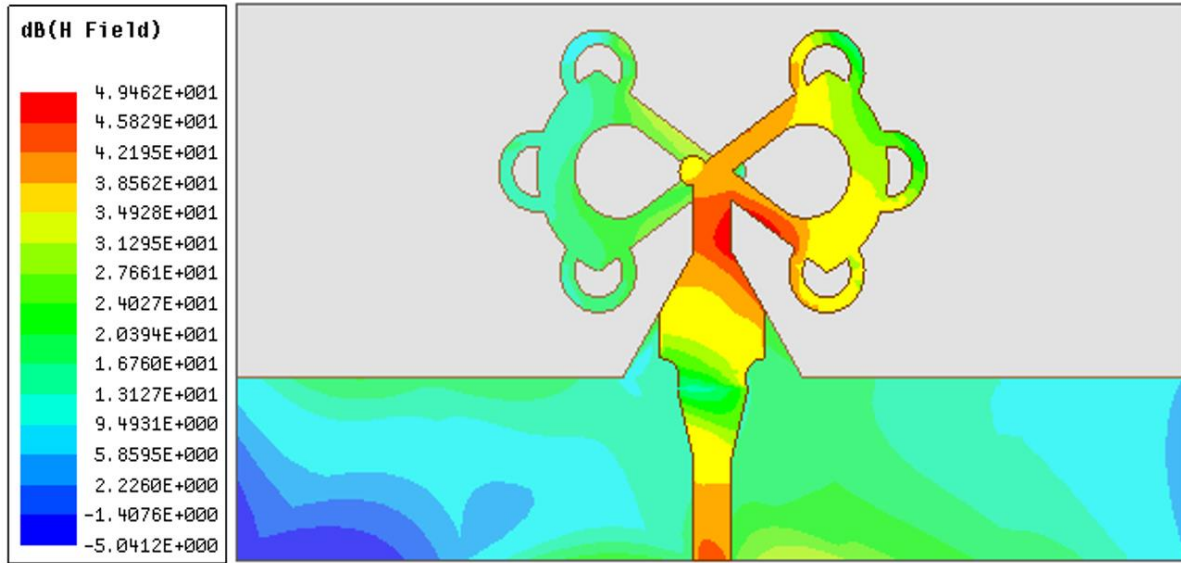


**Figure 5.4.** Simulated H-field distribution at 18.35 GHz frequency

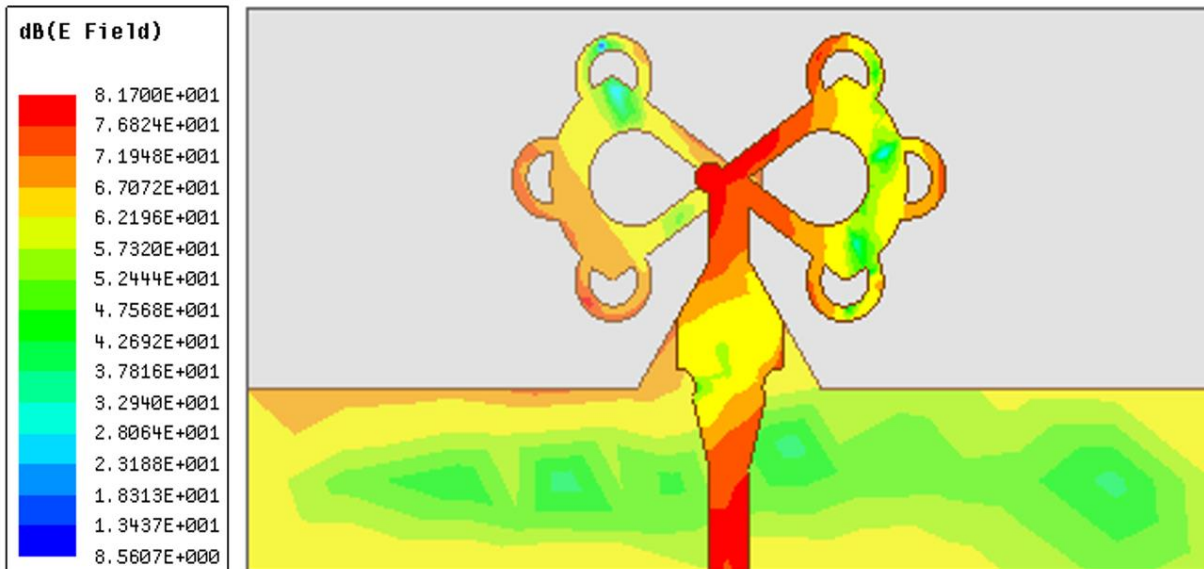


**Figure 5.5.** Simulated H-field distribution at 18.35 GHz frequency

The simulated 2D radiation patterns of the designed antenna are shown in Fig. 5.6 at 18.35 GHz frequency in the  $\phi=0$  and  $\phi=90$  planes. The cross-polarization values are lower than the co-polarized values.

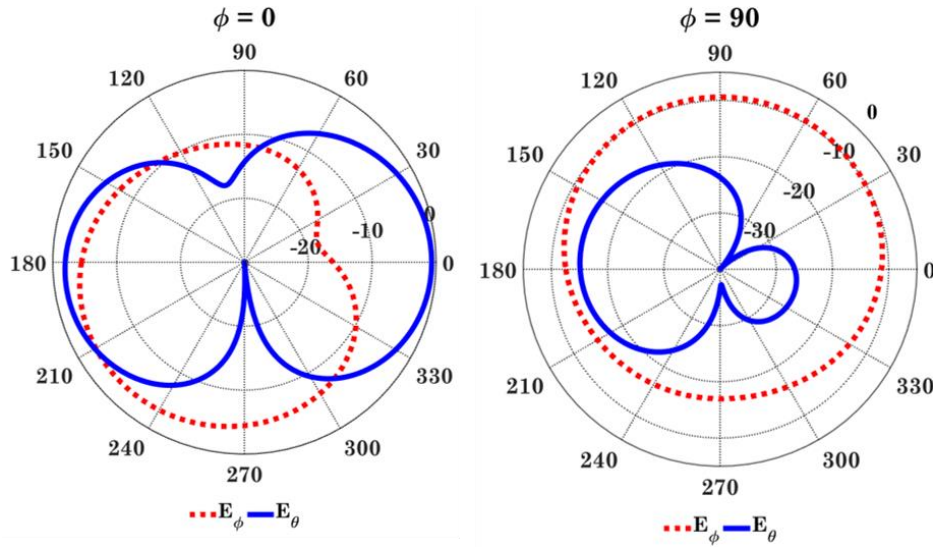


**Figure 5.6.** Simulated radiation pattern of the antenna at 18.35 GHz frequency for, (a)  $\phi=0$  and (b)  $\phi=90$  planes

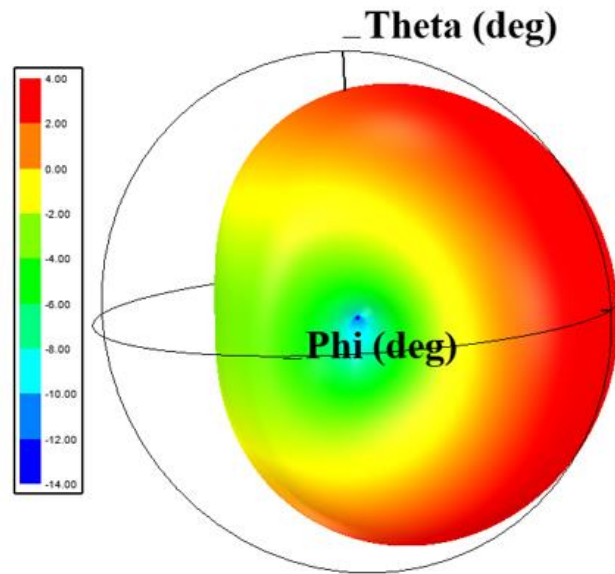


**Figure 5.7.** 3D simulated gain pattern of the proposed 5G antenna.

The 3D radiation pattern of this designed antenna at 18.35 GHz resonance frequency is shown in Fig. 5.7. Further, a comparable constant peak gain and radiation efficiency observed as 4 dBi and 90% for the entire frequency range.

### 5.3 The proposed beam-steerable antenna array design:

To make an antenna array, the number of elements need to consists of two or more. To investigate the distance,  $d$ , between the adjacent elements, a key factor on the antenna radiation performance [10], we started to design an array from two to eight similar elements, as presented in Fig. 5.8.

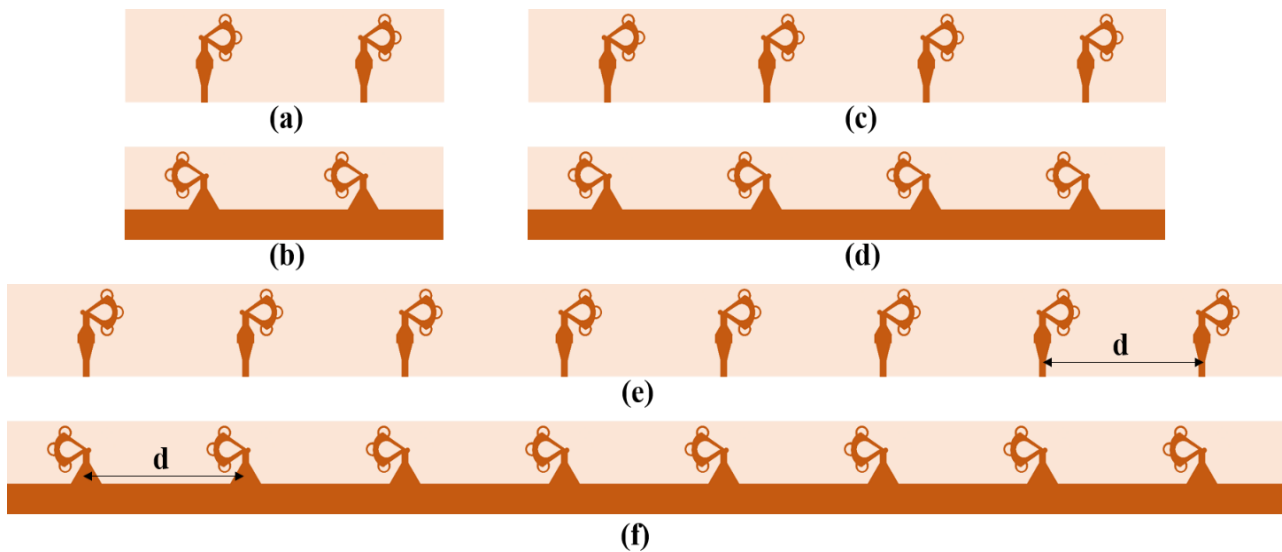


**Figure 5.8.** Geometry of the phased array antenna, (a) Top View, two elements array, (b) Bottom View, two elements array, (c) Top View, four elements array, (d) Bottom View, four elements array, (e) Top View, eight elements array, (f) Bottom View, eight elements

The simulated  $S_{21}$  characteristics of the eight elements array design for different values of  $d$  as a function of  $\lambda$ , the guided wavelength is illustrated in Fig. 5.9. According to this graph, it

appears that  $d$  must be equal or close to  $\lambda/2$  to obtain the low mutual coupling characteristics over its operating frequency range.

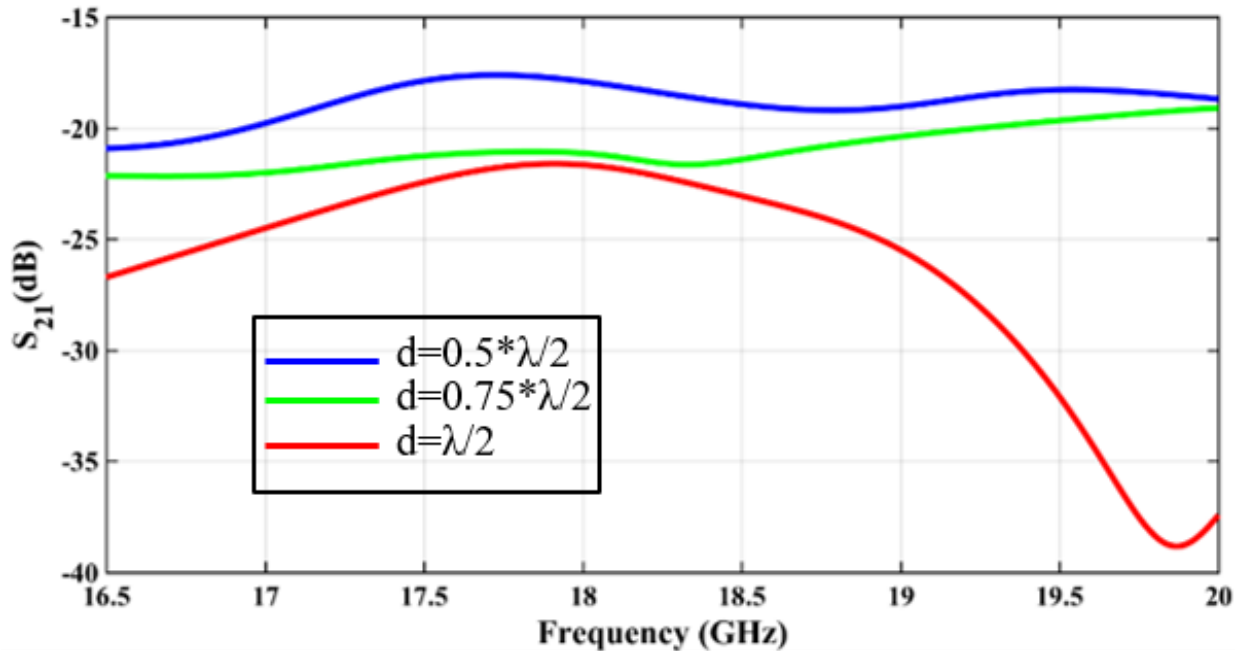


**Figure 5.9.**  $S_{21}$  characteristics of the eight element antenna for different values of  $d$

After many iterations in HFSS, we ended up the  $d$  value as 7.5 mm  $\sim \lambda/2$ , which yields a low mutual coupling effect, high gain, and high radiation efficiency. With this  $d$  value, the total dimension of the antenna components for two elements, four elements, and eight-element phased array antenna can be varied.

In order to obtain the high gain and wide scene of beam steering characteristics, we considered eight antenna elements in the proposed phased array design. The simulated S-parameters ( $S_{11}$  to  $S_{81}$ ) of the proposed array is presented in Fig. 5.10. It can be seen that the antenna array has quite good performance regarding the  $S_{11}$  parameter likewise a single element antenna within the entire frequency bandwidth 16.65-19.65 GHz (3 GHz) with return loss less than

-10 dB. Further, all mutual-coupling ( $S_{21}$  to  $S_{81}$ ) characteristics between the elements lie less than -20 dB, which follows the beam steering requirements perfectly.

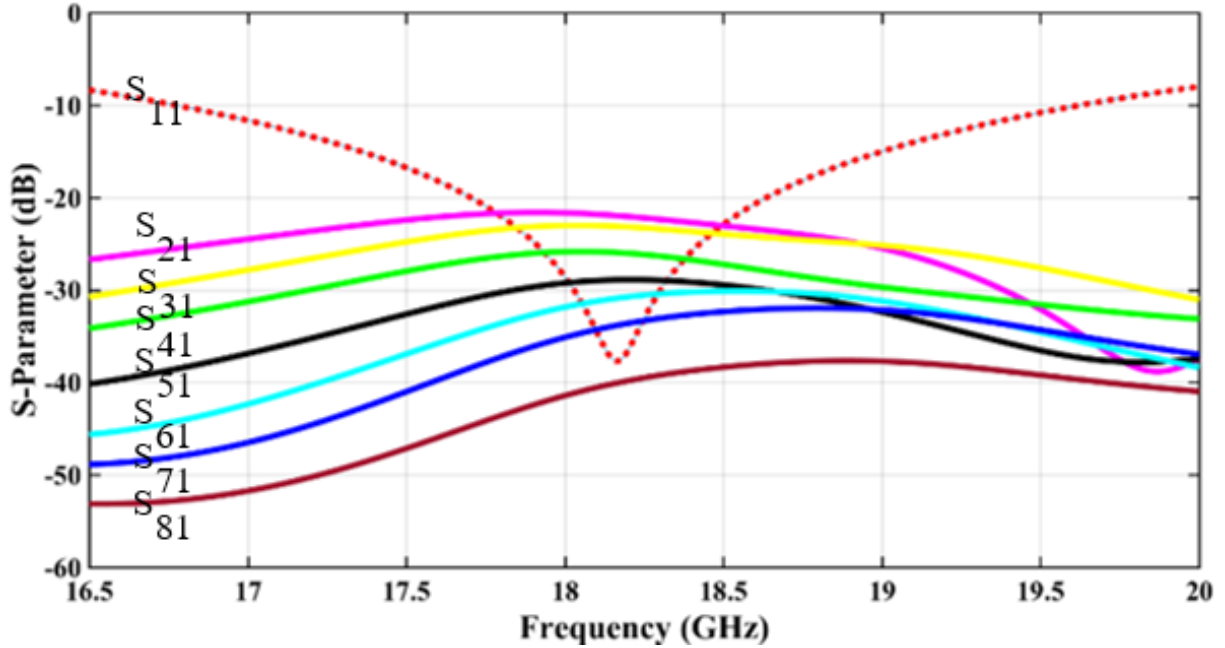


**Figure 5.10.** Simulated S parameters of proposed eight element antenna

In telecommunications, point-to-point communication between the base station and remote handheld devices are vital that can be ensured from the array beam forming and scanning characteristics. The simulated 3D and 2D directional radiation beam of the proposed 5G antenna at different scanning angles ( $0^\circ$ ,  $15^\circ$ ,  $30^\circ$ ,  $45^\circ$ ,  $60^\circ$ , and  $75^\circ$ ) at 18.35 GHz are shown in Fig. 5.11.

As observed, the side lobes are still small compared with the main lobes at all scanning angles that is an important criterion to evaluate the scanning property. As illustrated in Fig. 5.12, the proposed array has the almost symmetrical beam steering characteristics regarding gain, beam forming, and side lobes for the negative scanning angles ( $0^\circ$ ,  $-15^\circ$ ,  $-30^\circ$ ,  $-45^\circ$ ,  $-60^\circ$ , and  $-75^\circ$ ) as positive angles.

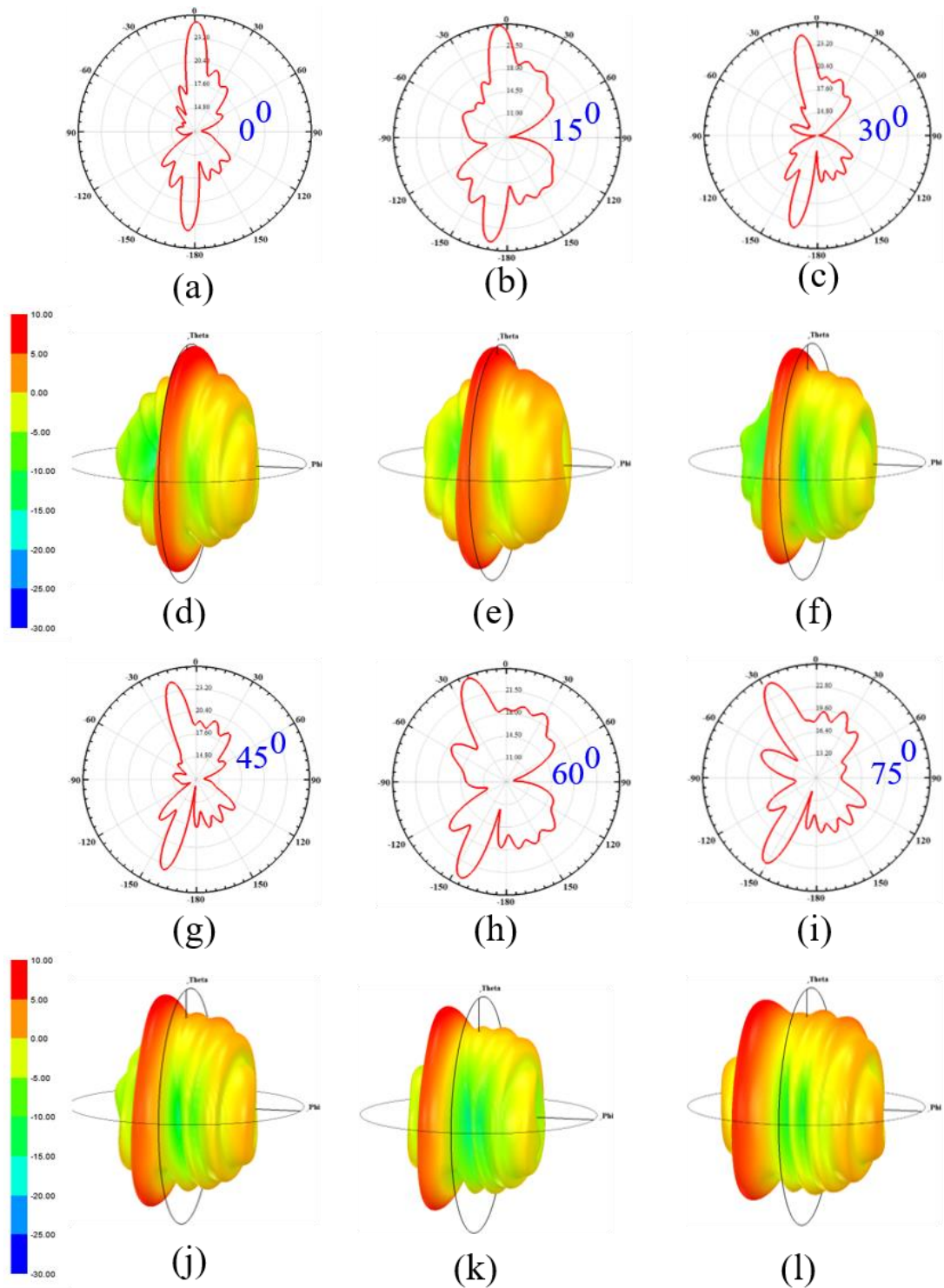


**Figure 5.11.** 2D radiation pattern and 3D gain of the proposed eight element array antenna at different positive scanning angles ( $0^\circ$ ,  $15^\circ$ ,  $30^\circ$ ,  $45^\circ$ ,  $60^\circ$ ,  $75^\circ$ ).

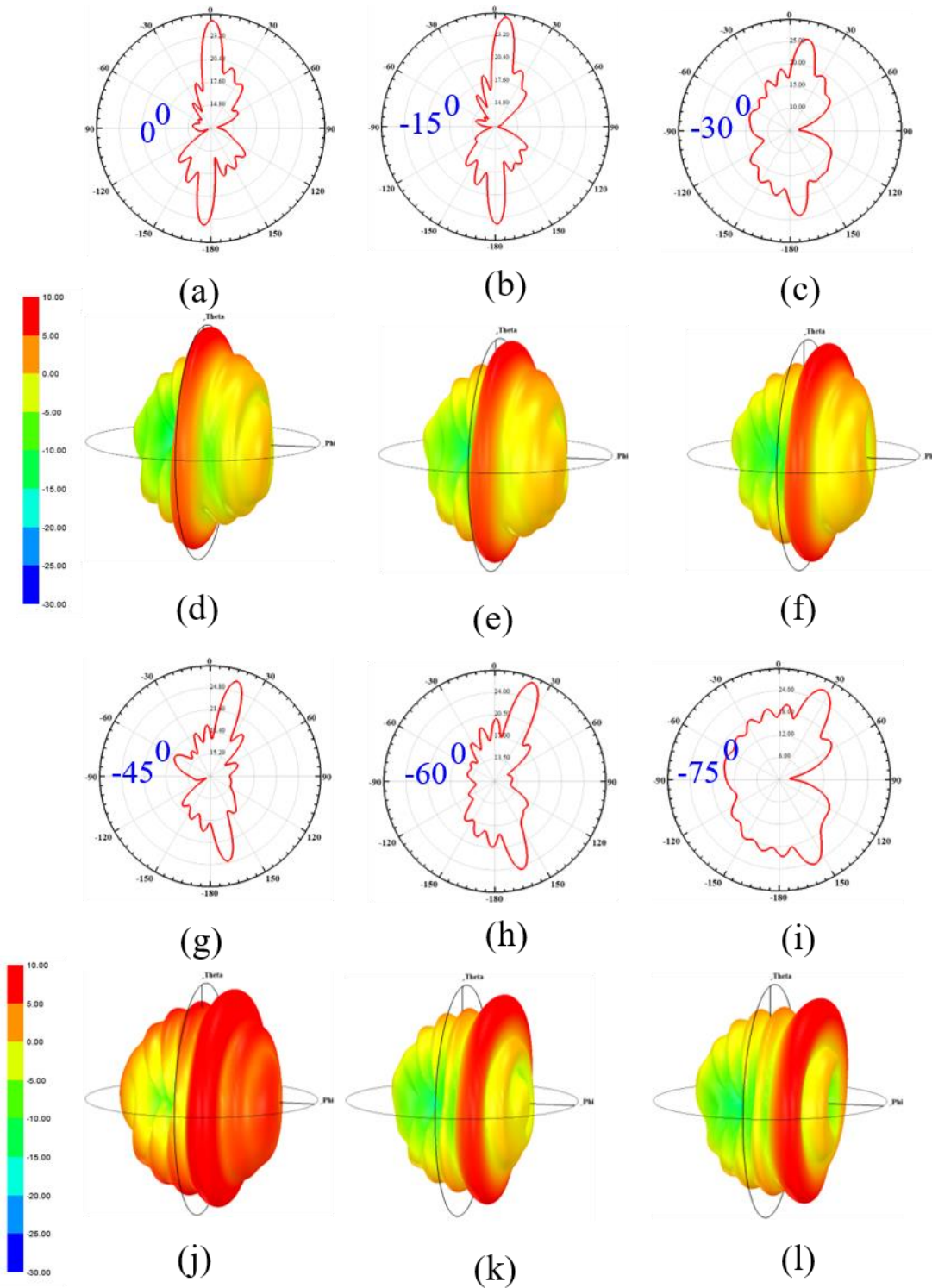


**Figure 5.12.** 2D radiation pattern and 3D gain of the proposed eight element array antenna at different positive scanning angles ( $0^\circ$ ,  $-15^\circ$ ,  $-30^\circ$ ,  $-45^\circ$ ,  $-60^\circ$ ,  $-75^\circ$ ).

It can be seen more clearly from the 2D results, presented in Fig. 5.13 for the negative scanning angles, where most of the side lobes lie below 0 dB level. Moreover, these results show seemingly good beam steering property with the end-fire mode and comparable high gain (around 8 dBi) values.

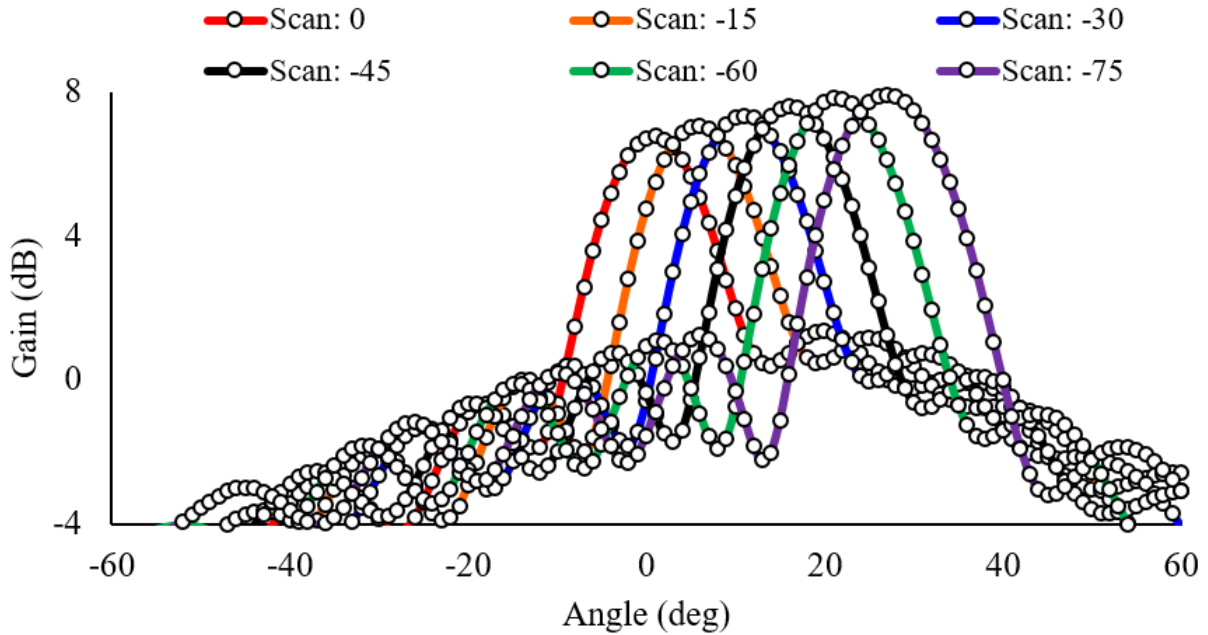


**Figure 5.13.** Simulated 2D radiation beams of the proposed antenna at 18.35 GHz frequency with different scan angles

Likewise, 1x8 elements array, we notice the similar bandwidth, mutual coupling, radiation and beam-steering results for the 1x2 and 1x4 elements array. However, the obtained gain was lower than the 1x8 elements array (5.2 dBi for 1x2 elements and 6.2 dBi for 1x4 elements). The gain values of the proposed array can be increased based on the system requirement after increasing the number of array elements.

## 5.4 Summary

A new design of compact modified bow-tie array antenna with beam steering characteristics is proposed in this project for 5G applications. The overall physical dimension of a single element antenna is 10 mm x 5.5 mm x 1.5 mm, with the conventional FR4 based substrate. To meet the 5G requirements, we employed eight elements at 18.35 GHz operating frequency to form a linear phased array. The proposed design is validated by FEM based simulations. The results show that this design offers several advantages including 1) larger bandwidth, 3 GHz with return loss  $< -10$  dB, 2) impedance matching, 3) good mutual coupling, insertion loss  $< -20$  dB, 4) high gain, 8 dBi, 5) radiation pattern and 6) beam steering characteristics over the entire frequency spectrum. Based on the mentioned attractive features, the proposed antenna can meet the need of future 5G communications.

## CHAPTER 6: CONCLUSIONS AND FUTURE WORK

An overview of both flexible and rigid substrates based high-performance antenna design has been presented in some detail in this chapter for future IoT and high-speed 5G communications.

The second chapter presented our approach to investigating the inkjet printing properties on photo paper applying silver nanoparticle ink. It discussed, how methodologies, materials, parameters, and post-processing technique propagate and affect the performance of the printed patterns in terms of conductivity. In this study, we statistically analyzed our experimented data using analysis of variances (ANOVA) to find out which factors are significant ( $p < 0.05$ ) to yield the best-printed outcome. According to the results achieved after many iterations and ANOVA analysis, printing at  $15\mu\text{m}$  drop spacing, maintaining two layers of ink deposition, and sintered at  $90^{\circ}\text{C}$  for 30 minutes gives the best conductivity on photo paper. Afterward, the repetitive bending test described that the printed patterns were unaffected when flexed around random diameters of cylindrical support indicating excellent stability under stress. Future work in this area will involve adhesion and chemical wet bench test to characterize the more robustness behaviors of the printed devices in any harsh conditions.

The third chapter described how our developed optimizing printing conditions were transferred to fabricate a UWB antenna over the photo paper. In this chapter, we explained a new UWB monopole antenna with CPW feeding technique. We completed the design, EM simulation, and experimentation portions from scratch and it operates over 3.2-30 GHz frequency spectrum. Our result showed relatively omnidirectional performances over the entire frequency spectrum and compliance with the FCC's UWB requirements. The mentioned performances and flexible characteristics of the paper substrate make it a suitable candidate for the commercial IoT

applications. In chapter four, we brought a relatively similar designed monopole antenna over the traditional FR4 substrates for the UWB applications. To achieve the UWB behavior, we considered a microstrip feeding method instead of CPW feeding technique. To validate the design and HFSS based simulation, we experimented the model which underscores both simulated and measured results are in good agreement. Our results indicated, this design on FR4 substrates operates over 4.0 to 40.0 GHz with six different operating bands, which suggests applying this model for multiservice wireless applications. With regards to the future work for both chapter 3 and 4, the proposed antenna can be simulated and tested with an anthropomorphic phantom forearm-hand and other devices or components.

In chapter five, we studied and simulated a new 5G phased array antenna at 18.35 GHz frequency with 3 GHz frequency bandwidth. The analysis includes design details of the single element antenna as well as two or more element based phased array elements. It showcases how gain values of the array antenna can be increased based on the system requirement or applications after increasing the number of array elements. Since our current 5G design is based on the simulation only, so the future works in this chapter will involve the experimentation at the FCC assigned operating frequency. Finally, for any designed antennas to comply with the requirements of many carriers, vendors, and regulatory bodies the fabricated design or systems can be passed through over-the-air (OTA) testing to predict the real-world wireless device reliability, safety and performance capabilities.

## REFERENCES

- [1] S. R. Zahran, M. A. Abdalla, and A. Gaafar, "Time domain analysis for foldable thin UWB monopole antenna," *AEU-International Journal of Electronics and Communications*, vol. 83, pp. 253-262, 2018.
- [2] J. Abu-Khalaf, R. Saraireh, S. Eisa, and A. a. Al-Halhouli, "Experimental characterization of inkjet-printed stretchable circuits for wearable sensor applications," *Sensors*, vol. 18, p. 3476, 2018.
- [3] T. Zhang, X. Wang, T. Li, Q. Guo, and J. Yang, "Fabrication of flexible copper-based electronics with high-resolution and high-conductivity on paper via inkjet printing," *Journal of Materials Chemistry C*, vol. 2, pp. 286-294, 2014.
- [4] G. A. Casula, G. Montisci, and G. Mazzarella, "A wideband PET inkjet-printed antenna for UHF RFID," *IEEE Antennas and Wireless Propagation Letters*, vol. 12, pp. 1400-1403, 2013.
- [5] S. Jung, A. Sou, K. Banger, D. H. Ko, P. C. Chow, C. R. McNeill, et al., "All-inkjet-printed, all-air-processed solar cells," *Advanced Energy Materials*, vol. 4, 2014.
- [6] S. K. Garlapati, N. Mishra, S. Dehm, R. Hahn, R. Kruk, H. Hahn, et al., "Electrolyte-gated, high mobility inorganic oxide transistors from printed metal halides," *ACS applied materials & interfaces*, vol. 5, pp. 11498-11502, 2013.
- [7] C. Hu, X. Bai, Y. Wang, W. Jin, X. Zhang, and S. Hu, "Inkjet printing of nanoporous gold electrode arrays on cellulose membranes for high-sensitive paper-like electrochemical

- oxygen sensors using ionic liquid electrolytes," *Analytical chemistry*, vol. 84, pp. 3745-3750, 2012.
- [8] J. Bohn, V. Coroamă, M. Langheinrich, F. Mattern, and M. Rohs, "Living in a world of smart everyday objects—social, economic, and ethical implications," *Human and Ecological Risk Assessment*, vol. 10, pp. 763-785, 2004.
- [9] A. Mansour, M. Azab, and N. Shehata, "Flexible paper-based wideband antenna for compact-size IoT devices," in *Information Technology, Electronics and Mobile Communication Conference (IEMCON), 2017 8th IEEE Annual*, 2017, pp. 426-429.
- [10] M. H. Novak and J. L. Volakis, "Ultrawideband antennas for multiband satellite communications at UHF–Ku frequencies," *IEEE Transactions on Antennas and Propagation*, vol. 63, pp. 1334-1341, 2015.
- [11] W. Roh, J.-Y. Seol, J. Park, B. Lee, J. Lee, Y. Kim, et al., "Millimeter-wave beamforming as an enabling technology for 5G cellular communications: Theoretical feasibility and prototype results," *IEEE communications magazine*, vol. 52, pp. 106-113, 2014.
- [12] N. Ojaroudiparchin, M. Shen, and G. F. Pedersen, "Investigation on the performance of low-profile insensitive antenna with improved radiation characteristics for the future 5G applications," *Microwave and Optical Technology Letters*, vol. 58, pp. 2148-2151, 2016.
- [13] D. C. Thompson, O. Tantot, H. Jallageas, G. E. Ponchak, M. M. Tentzeris, and J. Papapolymerou, "Characterization of liquid crystal polymer (LCP) material and transmission lines on LCP substrates from 30 to 110 GHz," *IEEE Transactions on Microwave Theory and Techniques*, vol. 52, pp. 1343-1352, 2004.

- [14] A. H. Rida, "Conductive inkjet printed antennas on flexible low-cost paper-based substrates for RFID and WSN applications," Georgia Institute of Technology, 2009.
- [15] K. Mandke, H. Nam, L. Yerramneni, C. Zuniga, and T. Rappaport, "The evolution of ultra wide band radio for wireless personal area networks," *Spectrum*, vol. 3, p. 10.6, 2003.
- [16] T. Kim, I. Bang, and D. K. Sung, "Design criteria on a mmWave-based small cell with directional antennas," in *2014 IEEE 25th Annual International Symposium on Personal, Indoor, and Mobile Radio Communication (PIMRC)*, 2014, pp. 103-107.
- [17] N. Arjona, S. Rivas, L. Álvarez-Contreras, M. Guerra-Balcázar, J. Ledesma-García, E. Kjeang, et al., "Glycerol electro-oxidation in alkaline media using Pt and Pd catalysts electrodeposited on three-dimensional porous carbon electrodes," *New Journal of Chemistry*, vol. 41, pp. 1854-1863, 2017.
- [18] P. Warrian and T. Southin, "The Internet of Things and Printed Electronics: Case Studies of Innovation by SME Manufacturers," *Global Journal of Management And Business Research*, 2017.
- [19] N. Komoda, M. Nogi, K. Suganuma, H. Koga, and K. Otsuka, "Silver nanowire antenna printed on polymer and paper substrates," in *2012 12th IEEE International Conference on Nanotechnology (IEEE-NANO)*, 2012, pp. 1-5.
- [20] M. M. Tentzeris, S. Kim, A. Traille, H. Aubert, K. Yoshihiro, A. Georgiadis, et al., "Inkjet-printed RFID-enabled sensors on paper for IoT and "Smart Skin" applications," in *ICECom 2013*, 2013, pp. 1-4.

- [21] S. Ali, J. Bae, and C. H. Lee, "Design of versatile printed organic resistor based on resistivity ( $\rho$ ) control," *Applied Physics A*, vol. 119, pp. 1499-1506, 2015.
- [22] E. Cantatore, T. C. Geuns, G. H. Gelinck, E. van Veenendaal, A. F. Gruijthuijsen, L. Schrijnemakers, et al., "A 13.56-MHz RFID system based on organic transponders," *IEEE Journal of solid-state circuits*, vol. 42, pp. 84-92, 2007.
- [23] I. Pandey, J. D. Tiwari, T. K. Saha, A. Khosla, H. Furukawa, and P. K. Sekhar, "Black carbon paper based polyanthraquinone coated exfoliated graphite for flexible paper battery," *Microsystem Technologies*, pp. 1-9.
- [24] G. Shaker, S. Safavi-Naeini, N. Sangary, and M. M. Tentzeris, "Inkjet printing of ultrawideband (UWB) antennas on paper-based substrates," *IEEE Antennas and Wireless Propagation Letters*, vol. 10, pp. 111-114, 2011.
- [25] A. Abbas and I. Bajwa, "Inkjet Printing of Ag Nanoparticles using Dimatix Inkjet Printer, No 1," 2017.
- [26] L. Yang, A. Rida, R. Vyas, and M. M. Tentzeris, "RFID tag and RF structures on a paper substrate using inkjet-printing technology," *IEEE Transactions on Microwave Theory and Techniques*, vol. 55, pp. 2894-2901, 2007.
- [27] F. L. Wignes, C. Glascoe, G. Makar, T. Karakolak, and P. Sekhar, "A paper based 2-element antenna for WLAN MIMO applications fabricated using inkjet technology," *Microwave and Optical Technology Letters*, vol. 59, pp. 2785-2790, 2017.

- [28] W. Cui, W. Lu, Y. Zhang, G. Lin, T. Wei, and L. Jiang, "Gold nanoparticle ink suitable for electric-conductive pattern fabrication using ink-jet printing technology," *Colloids and Surfaces A: Physicochemical and Engineering Aspects*, vol. 358, pp. 35-41, 2010.
- [29] S. Lim, M. Joyce, P. D. Fleming, A. T. Aijazi, and M. Atashbar, "Inkjet printing and sintering of nano-copper ink," *Journal of Imaging Science and Technology*, vol. 57, pp. 50506-1-50506-7, 2013.
- [30] A. Hassan, S. Ali, G. Hassan, J. Bae, and C. H. Lee, "Inkjet-printed antenna on thin PET substrate for dual band Wi-Fi communications," *Microsystem Technologies*, vol. 23, pp. 3701-3709, 2017.
- [31] Q. Huang, W. Shen, Q. Xu, R. Tan, and W. Song, "Properties of polyacrylic acid-coated silver nanoparticle ink for inkjet printing conductive tracks on paper with high conductivity," *Materials Chemistry and Physics*, vol. 147, pp. 550-556, 2014.
- [32] T. Öhlund, A. Schuppert, B. Andres, H. Andersson, S. Forsberg, W. Schmidt, et al., "Assisted sintering of silver nanoparticle inkjet ink on paper with active coatings," *RSC Advances*, vol. 5, pp. 64841-64849, 2015.
- [33] S. Li, X. He, J. Hao, J. Zhou, and F. Xue, "Investigation of properties and curing process of silver paste electrically conductive adhesives (ECAs)," in *2017 18th International Conference on Electronic Packaging Technology (ICEPT)*, 2017, pp. 275-279.
- [34] N. Raut and K. Al-Shamery, "Inkjet printing metals on flexible materials for plastic and paper electronics," *Journal of Materials Chemistry C*, vol. 6, pp. 1618-1641, 2018.

- [35] M. Y. Chuang, "Inkjet Printing of Ag Nanoparticles using Dimatix Inkjet Printer, No 2," 2017.
- [36] Y. Fang, L. Li, Z. Xin, and W. Zhao, "Research on conductive performance of inkjet printing samples by conductive inkjet ink," in 2009 3rd IEEE International Symposium on Microwave, Antenna, Propagation and EMC Technologies for Wireless Communications, 2009, pp. 63-66.
- [37] J. Hao, X. He, S. Li, J. Zhou, and F. Xue, "The effect of curing agent on the properties of silver paste Electrically Conductive Adhesives (ECAs)," in 2017 18th International Conference on Electronic Packaging Technology (ICEPT), 2017, pp. 644-648.
- [38] A. Kamyshny, J. Steinke, and S. Magdassi, "Metal-based inkjet inks for printed electronics," *The Open Applied Physics Journal*, vol. 4, 2011.
- [39] K. Janeczek, G. Kozioł, T. Serzysko, and M. Jakubowska, "Investigation of RFID tag antennas printed on flexible substrates using two types of conductive pastes," in 3rd Electronics System Integration Technology Conference ESTC, 2010, pp. 1-5.
- [40] D. E. Anagnostou, A. A. Gheethan, A. K. Amert, and K. W. Whites, "A direct-write printed antenna on paper-based organic substrate for flexible displays and WLAN applications," *Journal of Display Technology*, vol. 6, pp. 558-564, 2010.
- [41] J. Sidén, M. Fein, A. Koptug, and H.-E. Nilsson, "Printed antennas with variable conductive ink layer thickness," *IET Microwaves, Antennas & Propagation*, vol. 1, pp. 401-407, 2007.

- [42] D. Kim and J. Moon, "Highly conductive ink jet printed films of nanosilver particles for printable electronics," *Electrochemical and Solid-State Letters*, vol. 8, pp. J30-J33, 2005.
- [43] F. FCC and D. FCC, "1st report and order on ultrawideband technology," FCC, Washington, DC, 2002.
- [44] M. Nejatijahromi, M. Naghshvarianjahromi, and M. Rahman, "Switchable Planar Monopole Antenna Between Ultra-Wideband and Narrow Band Behavior," *Progress In Electromagnetics Research*, vol. 75, pp. 131-137, 2018.
- [45] S. M. Hamza, F. A. Tahir, and H. M. Cheema, "A high-gain inkjet-printed UWB LPDA antenna on paper substrate," *International Journal of Microwave and Wireless Technologies*, vol. 9, pp. 931-937, 2017.
- [46] G. Geetha, S. K. Palaniswamy, M. G. N. Alsath, M. Kanagasabai, and T. R. Rao, "Compact and Flexible Monopole Antenna for Ultra-Wideband Applications Deploying Fractal Geometry," *Journal of Electrical Engineering & Technology*, vol. 13, pp. 400-405, 2018.
- [47] L. J. Xu, H. Wang, Y. Chang, and Y. Bo, "A flexible UWB inverted-F antenna for wearable application," *Microwave and Optical Technology Letters*, vol. 59, pp. 2514-2518, 2017.
- [48] B. N. Balarami Reddy, P. Sandeep Kumar, T. Rama Rao, N. Tiwari, and M. Balachary, "Design and Analysis of Wideband Monopole Antennas for Flexible/Wearable Wireless Device Applications," *Progress In Electromagnetics Research*, vol. 62, pp. 167-174, 2017.
- [49] H. R. Khaleel, H. M. Al-Rizzo, D. G. Rucker, and S. Mohan, "A compact polyimide-based UWB antenna for flexible electronics," *IEEE Antennas and Wireless Propagation Letters*, vol. 11, pp. 564-567, 2012.

- [50] M. Karimyian-Mohammadabadi, M. Dorostkar, F. Shokuohi, M. Shanbeh, and A. Torkan, "Super-wideband textile fractal antenna for wireless body area networks," *Journal of Electromagnetic Waves and Applications*, vol. 29, pp. 1728-1740, 2015.
- [51] Q. Fu, M. Nie, Q. Wu, J. Yang, and R. Li, "Direct-writing on paper of CPW-fed slot antenna with silver nanowire conductive ink," in *2018 IEEE International Conference on Computer and Communication Engineering Technology (CCET)*, 2018, pp. 128-132.
- [52] H. Phan, T. Vuong, P. Benech, P. Xavier, P. Borel, and A. Delattre, "Novel ultra-wideband "robe" antenna on high-loss paper substrate," in *Antennas and Propagation & USNC/URSI National Radio Science Meeting, 2017 IEEE International Symposium on*, 2017, pp. 319-320.
- [53] H. P. Phan, T.-P. Vuong, P. Benech, P. X. P. Borel, and A. Delattre, "Low-cost wideband antenna on paper substrate," in *2017 11th European Conference on Antennas and Propagation (EUCAP)*, 2017, pp. 2168-2171.
- [54] A. I. Hammoodi, M. Milanova, and H. Khaleel, "Design of Flexible Antenna for UWB Wireless Applications Using ANN," in *2017 International Conference on Computational Science and Computational Intelligence (CSCI)*, 2017, pp. 751-754.
- [55] M. U. Memon, M. M. Tentzeris, and S. Lim, "Inkjet-printed 3D Hilbert-curve fractal antennas for VHF band," *Microwave and Optical Technology Letters*, vol. 59, pp. 1698-1704, 2017.

- [56] W. A. Ali and A. A. Ibrahim, "A compact double-sided MIMO antenna with an improved isolation for UWB applications," *AEU-International Journal of Electronics and Communications*, vol. 82, pp. 7-13, 2017.
- [57] A. B. Constantine, "Antenna theory: analysis and design," *MICROSTRIP ANTENNAS*, third edition, John wiley & sons, 2005.
- [58] T. K. Saha, T. N. Knaus, A. Khosla, and P. K. Sekhar, "Investigation of Printing Properties on Paper Substrate," *Journal of The Electrochemical Society*, vol. 165, pp. B3163-B3167, 2018.
- [59] S. Singhal and A. K. Singh, "CPW-fed hexagonal Sierpinski super wideband fractal antenna," *IET Microwaves, Antennas & Propagation*, vol. 10, pp. 1701-1707, 2016.
- [60] T. K. Saha, C. Goodbody, T. Karacolak, and P. K. Sekhar, "A compact monopole antenna for ultra-wideband applications," *Microwave and Optical Technology Letters*.
- [61] R. Kumar and S. Gaikwad, "On the design of nano-arm fractal antenna for UWB wireless applications," *Journal of Microwaves, Optoelectronics and Electromagnetic Applications*, vol. 12, pp. 158-171, 2013.
- [62] R. K. Singh and D. Pujara, "Design of an UWB (2.1–38.6 GHz) circular microstrip antenna," *Microwave and Optical Technology Letters*, vol. 59, pp. 2762-2767, 2017.
- [63] X. L. Liang, "Ultra-wideband antenna and design," in *Ultra Wideband-Current Status and Future Trends*, ed: InTech, 2012.
- [64] J. R. James, P. S. Hall, and C. Wood, *Microstrip antenna: Theory and design: Iet*, 1981.

- [65] M. Peyrot-Solis, G. Galvan-Tejada, and H. Jardon-Aguilar, "A novel planar UWB monopole antenna formed on a printed circuit board," *Microwave and optical technology letters*, vol. 48, pp. 933-935, 2006.
- [66] P. Ranjan, S. Raj, G. Upadhyay, S. Tripathi, and V. S. Tripathi, "Circularly slotted flower shaped UWB filtering antenna with high peak gain performance," *AEU-International Journal of Electronics and Communications*, vol. 81, pp. 209-217, 2017.
- [67] D. M. Elsheakh and E. A. Abdallah, "Ultra-wide-bandwidth (UWB) microstrip monopole antenna using split ring resonator (SRR) structure," *International Journal of Microwave and Wireless Technologies*, pp. 1-10, 2018.
- [68] K.-R. Chen and J.-S. Row, "A compact monopole antenna for super wideband applications," *IEEE Antennas and Wireless Propagation Letters*, vol. 10, pp. 488-491, 2011.
- [69] M. Manohar, R. S. Kshetrimayum, and A. K. Gogoi, "Printed monopole antenna with tapered feed line, feed region and patch for super wideband applications," *IET Microwaves, Antennas & Propagation*, vol. 8, pp. 39-45, 2014.
- [70] R. Chandel, A. K. Gautam, and K. Rambabu, "Tapered fed compact UWB MIMO-diversity antenna with dual band-notched characteristics," *IEEE Transactions on Antennas and Propagation*, vol. 66, pp. 1677-1684, 2018.
- [71] T. M. Das, G. Sen, S. N. Islam, and S. Das, "A semi circular shaped UWB body area network antenna with C-band and WLAN band rejection," in *2018 Emerging Trends in Electronic Devices and Computational Techniques (EDCT)*, 2018, pp. 1-3.

- [72] R. Xu, J. Li, J. Liu, S. G. Zhou, and K. Wei, "UWB circularly polarised slot antenna with modified ground plane and L-shaped radiator," *Electronics Letters*, vol. 54, pp. 918-920, 2018.
- [73] J. S. Sun, Y. C. Lee, and S. C. Lin, "New design of a CPW-fed ultrawideband slot antenna," *Microwave and Optical Technology Letters*, vol. 49, pp. 561-564, 2007.
- [74] M. Mokhtaari and J. Bornemann, "Printed-circuit antennas for ultra-wideband monitoring applications," in *Electromagnetic Compatibility (APEMC), 2012 Asia-Pacific Symposium on, 2012*, pp. 157-160.
- [75] A. Azari, "A new super wideband fractal microstrip antenna," *IEEE transactions on antennas and propagation*, vol. 59, pp. 1724-1727, 2011.
- [76] J. Liu, S. Zhong, and K. P. Esselle, "A printed elliptical monopole antenna with modified feeding structure for bandwidth enhancement," *IEEE Transactions on Antennas and Propagation*, vol. 59, pp. 667-670, 2011.
- [77] M. N. Rahman, M. T. Islam, M. S. J. Singh, N. Misran, K. Mat, and M. Samsuzzaman, "Compact microstrip patch antenna for multi-service wireless communications," in *Microwave Conference (APMC), 2017 IEEE Asia Pacific, 2017*, pp. 1048-1050.
- [78] E. G. Lim, Z. Wang, G. Juans, K. L. Man, N. Zhang, V. Hananov, et al., "Design and optimization of a planar UWB antenna," in *East-West Design & Test Symposium, 2013, 2013*, pp. 1-5.

- [79] S. U. Rahman, Q. Cao, Y. Li, I. Gil, and W. Yi, "Design of tri-notched UWB antenna based on elliptical and circular ring resonators," *International Journal of RF and Microwave Computer-Aided Engineering*, vol. 29, p. e21648, 2019.
- [80] D. Subpart, "FEDERAL COMMUNICATIONS COMMISSION 47 CFR Part."
- [81] N. Ojaroudiparchin, M. Shen, and G. F. Pedersen, "Beam-steerable microstrip-fed bow-tie antenna array for fifth generation cellular communications," in *Antennas and Propagation (EuCAP), 2016 10th European Conference on*, 2016, pp. 1-5.
- [82] M. Peng and A. Zhao, "High performance 5G millimeter-wave antenna array for 37–40 GHz mobile application," in *2018 International Workshop on Antenna Technology (iWAT)*, 2018, pp. 1-4.
- [83] N. Ojaroudiparchin, M. Shen, and G. Fr, "Design of Vivaldi antenna array with end-fire beam steering function for 5G mobile terminals," in *Telecommunications Forum Telfor (TELFOR), 2015 23rd*, 2015, pp. 587-590.
- [84] M. Khalily, R. Tafazolli, P. Xiao, and A. A. Kishk, "Broadband mm-wave microstrip array antenna with improved radiation characteristics for different 5G applications," *IEEE Transactions on Antennas and Propagation*, vol. 66, pp. 4641-4647, 2018.
- [85] S. Zhang, I. Syrytsin, and G. F. Pedersen, "Compact Beam-Steerable Antenna Array With Two Passive Parasitic Elements for 5G Mobile Terminals at 28 GHz," *IEEE Transactions on Antennas and Propagation*, vol. 66, pp. 5193-5203, 2018.